Research Square

Preprints are preliminary reports that have not undergone peer review.
They should not be considered conclusive, used to inform clinical practice,
or referenced by the media as validated information.

Fluorite recognized as the principal source mineral for regolith-hosted HREE deposits

Wei Jian

weijian851@gmail.com

China University of Geosciences (Beijing)

Shida Zhai

China University of Geosciences (Beijing)

Jingwen Mao

China University of Geosciences (Beijing) https://orcid.org/0000-0002-1386-2799

Bernd Lehmann

Technical University of Clausthal https://orcid.org/0000-0003-0762-6543

Nian Chen

China University of Geosciences (Beijing)

Shiwei Song

China University of Geosciences (Beijing)

Min Liu

China University of Geosciences (Beijing)

Xuyang Meng

China University of Geosciences (Beijing)

Xianguang Wang

Jiangxi Mineral Resources Guarantee Service Center

Liangxin Gong

Jiangxi Nonferrous Geological Mineral Exploration and Development Institute

Guogang Ren

Key Laboratory of Ionic Rare Earth Resources and Environment, Ministry of Natural Resources of the People's Republic of China

Adam Simon

University of Michigan https://orcid.org/0000-0002-1733-5718

Article

Keywords:

Posted Date: March 3rd, 2026

DOI: https://doi.org/10.21203/rs.3.rs-8880973/v1

License: This work is licensed under a Creative Commons Attribution 4.0 International License.
Read Full License

Additional Declarations: There is **NO** Competing Interest.

Fluorite recognized as the principal source mineral for regolith-hosted HREE deposits

Shida Zhai[1,2,3], Wei Jian[1]*, Jingwen Mao[3]*, Bernd Lehmann[4], Nian Chen1, Shiwei Song[1], Min Liu[1], Xuyang Meng[1], Xianguang Wang[5], Liangxin Gong[6], Guogang Ren[2], Adam C. Simon[7]

[1]MNR Key Laboratory for Exploration Theory and Technology of Critical Mineral Resources, China University of Geosciences (Beijing), Beijing, China.

[2]Key Laboratory of Ionic Rare Earth Resources and Environment, Ministry of Natural Resources of the People's Republic of China, Ganzhou, China.

[3]MNR Key Laboratory of Metallogeny and Mineral Assessment, Institute of Mineral Resources, Chinese Academy of Geological Sciences, Beijing, China.

[4]Mineral Resources, Technische Universität Clausthal, Clausthal-Zellerfeld, Germany.

[5]Jiangxi Mineral Resources Guarantee Service Center, Nanchang, China.

[6]Jiangxi Nonferrous Geological Mineral Exploration and Development Institute, Nanchang, China.

[7]Earth & Environmental Sciences, University of Michigan, Ann Arbor, MI, USA.

*Corresponding author. Email: jianwei@cugb.edu.cn (W.J.); jingwenmao@263.net (J.W.M.)

Regolith-hosted rare earth element (REE) deposits in South China supply most of the world's heavy REE (HREE), but the parent minerals that liberate HREE during weathering remain uncertain because commonly invoked accessory phases are refractory. Here we recognize that fluorite is the dominant HREE host in the granitic bedrock of the world's largest deposit (Shitouping; ~174,000 t HREE oxides). Fluorite occurs in the Early Cretaceous syenogranite at a concentration of ~0.8 wt.% and contains 4.7 wt.% REE with a LREE/HREE ratio of 0.3, accounting for 82% of the bulk-rock HREE budget. During supergene weathering, fluorite dissolves almost completely (> 99%), releasing HREE that adsorb onto clay minerals in the overlying

saprolite, whereas refractory phases such as xenotime persist. Mass-balance modelling confirms that HREE ions liberated from primary magmatic fluorite constitute the principal source of the economic ore. Extreme magmatic fractionation enriches residual melts in fluorine and HREE, driving fluorite crystallization and preferential HREE incorporation. Our results imply that regolith-hosted HREE deposits require bedrocks enriched in easily weathered HREE phases (notably fluorite) and depleted in refractory HREE hosts (e.g., xenotime and titanite), guiding exploration to F-rich, highly fractionated granites low in P and Ti.

Rare earth elements (REE) are indispensable to advanced technologies—permanent magnets, catalysts and high-end electronics[1,2]. Driven by the rapid expansion of renewable-energy and high-technology sectors, demand for REE—especially heavy REE (HREE: Gd–Lu and Y)—has surged in recent years owing to the greater scarcity of heavy relative to light REE (LREE: La–Eu) resources[3–5].

Regolith-hosted heavy rare earth elements (HREE) deposits in South China supply over 80 % of the world's HREE (Fig. 1)[6]. In these deposits, HREE are retained in the weathering profiles of granitic bedrocks as adsorbed ions on clay mineral surfaces (e.g., kaolinite and halloysite)[4,7]. These ions are believed to be liberated during in-situ weathering by the dissolution of primary HREE-bearing accessory minerals, such as xenotime, zircon, titanite, and synchysite[8–10], or secondary unnamed HREE minerals[3]. However, highly refractory minerals (e.g., xenotime, zircon, and titanite) predominantly persist as residual phases in the regolith[11], whereas the abundance of potentially labile minerals and their quantitative contribution to regolith-hosted HREE ores remain unconstrained[3].

Fluorite is a ubiquitous accessory mineral in highly fractionated granites (SiO_2 > 70 wt.%)[12,13] that are spatially and genetically linked to regolith-hosted HREE deposits in the Nanling Region of South China[9,14,15]. Notable examples include the granites of the Zudong and Dabu HREE deposits (Extended Data Fig. 1)[15,16]. Although fluorite has been reported in these granites[9,14,17,18], its contribution to the HREE budget of these deposits has not been evaluated.

Here, we document exceptionally HREE-rich fluorite from the granitic bedrock of the Shitouping deposit—the world's largest regolith-hosted HREE deposit, hosting ~174,000 metric tons (t) HREE oxides and ~9,300 t LREE oxides. We propose that fluorite is the principal parent mineral for HREE mineralization at Shitouping and, by extension, in analogous global regolith-hosted HREE deposits formed by chemical weathering of highly fractionated granites.

HREE distribution in bedrock and weathering profile

The Shitouping regolith-hosted HREE deposit is located in the eastern Nanling Region in South China, which hosts world's largest concentration of regolith-hosted HREE deposits (Extended Data Fig. 1)[3,8,19]. The HREE deposits overlie an Early Cretaceous (~140 Ma) syenogranite[20], which was the bedrock for the regolith-hosted HREE mineralization (Fig. 2, a,b, and Extended Data Fig. 2). The syenogranite consists of ~47 wt.% quartz, ~25 wt.% orthoclase, ~17 wt.% albite, and ~3 wt.% biotite (Extended Data Fig. 3), contains ~497 ppm REE (with ~272 ppm HREE), and an average LREE/HREE ratio of 0.8 (Extended Data Fig. 4).

HREE in the syenogranite are sequestered in accessory minerals such as fluorite, zircon, synchysite, columbite, thorite, samarskite, and xenotime (Fig. 2c). Fluorite accounts for ~0.8 wt. % of the syenogranite and is the dominant HREE-bearing mineral in the syenogranite (Fig. 2c and Extended Data Fig. 3). Fluorite appears as purple, euhedral to subhedral grains (100–800 μm), disseminated throughout the syenogranite (Extended Data Figs. 3 and 5). Backscattered electron imaging reveals that fluorite crystals consist of a bright, REE-enriched core (Flr-I) and a dark, REE-depleted domain (Flr-II) that occurs as rims around Flr-I or along microfractures (Fig. 3a,b, and Extended Data Fig. 6). Fluorite-I is generally homogeneou, whereas Flr-II exhibits a porous texture and hosts abundant, lath-shaped synchysite inclusions (Fig. 3a,b). This textural relationship implies that Flr-II and synchysite formed by coupled dissolution - reprecipitation of Flr-I during chemical weathering. Electron probe microanalyzer (EPMA) data indicate that Flr-I contains 0.8–7.2 wt.% REE, avg. 4.7 wt.%, with an LREE/HREE ratio of 0.1–1.1, avg. 0.3 (Fig. 3d). In contrast, Flr-II is characterized by a marked reduction in REE (0.3–2.8 wt.%, avg. 1.1) and a modest increase in the ratio of LREE/HREE (0.1–1.1, avg. 0.4). Synchysite contains ~43.2 wt.% REE and exhibits an average LREE/HREE ratio of 1.4 (Fig. 3d and Extended Data Fig. 6). Combined TESCAN Integrated Mineral Analyzer (TIMA) and EPMA data reveal that Flr-I and its alteration products Flr-II and synchysite contain 82 % of the HREE of the total syenogranite budget (Fig. 4). Mass balance modeling demonstrates that REE hosted in

Flr-II and synchysite were mobilized from primary Flr-I, without REE input from late-stage fluids (methods section 5). Flr-I occurs as disseminated grains in the syenogranite, rather than as open-fracture infillings. It is intergrown with magmatic biotite and feldspar and locally occurs as inclusions within these phases. These textural relationships (Extended Data Figs. 3 and 5), together with its trace-element signature (e.g., Tb/Ca versus Tb/La; fig. S7)[21,22], indicate that Flr-I crystallized directly from the melt[12]. Accessory HREE-bearing minerals other than fluorite constitute less than 0.1 wt.% of the syenogranite (Fig. 2c). Hence, while xenotime contains 50.4 wt.% HREE, it occurs in trace abundance and accounts for only ~7% of the total HREE budget of the syenogranite (Fig. 4).

The regolith profile above the syenogranite bedrock is comprised of, from bottom to surface, saprock (0.2–11 m in thickness), saprolite (1.6–26 m in thickness), and pedolith (0–2 m in thickness). Saprolite, the principal orebody (Fig. 2a)[15], hosts ~1,020 ppm REE and ~700 ppm HREE, with an average LREE/HREE ratio of ~0.48 (Extended Data Fig. 4). Chemical weathering of the syenogranite bedrock to saprolite reduced the abundance of fluorite and synchysite by ~99 % and ~95 %, respectively (Fig. 2c). In contrast, the abundances of refractory xenotime increased by ~83 % during chemical weathering of the bedrock to saprolite (Fig. 3c), and REE concentrations of xenotime remain essentially constant (Fig. 3d,e).

Fluorite as the source mineral for regolith-hosted HREE ores

The fluorite (CaF_2) lattice can readily accommodate REE because their ionic radii closely match that of Ca[23]. Moreover, fluorite preferentially incorporates HREE relative to LREE, making it an efficient HREE host[24,25]. Fluorite also dissolves rapidly under supergene weathering conditions (Fig. 2c). Collectively, these characteristics — combined with the near-ubiquitous occurrence of fluorite in highly fractionated granitic rocks — establish it as a compelling primary source of HREE for regolith-hosted deposits formed through chemical weathering of such bedrocks.

The almost complete removal of fluorite and synchysite from bedrock to saprolite (Fig. 2c) records extensive dissolution of both minerals during supergene weathering

by groundwater. This, coupled with fluorite accounting for 82 % of the total HREE content of the granite bedrock, demonstrates that HREE ions liberated from primary magmatic fluorite are the source for the regolith-hosted HREE saprolite ores. This is further supported by the markedly higher dissolution kinetics of fluorite under supergene weathering conditions compared to refractory HREE-bearing minerals such as xenotime. Experimental data demonstrate that fluorite, in the presence of low-temperature (~25 °C) mildly acidic (pH 5) water, dissolves about 10^{-5}–10^{-4} mol m^{-2} s^{-1}[26], which is 7 to 9 orders of magnitude faster than xenotime dissolves (10^{-13}–10^{-12} mol m^{-2} s^{-1}) in water at such conditions[27].

To further assess REE mineral dissolution in groundwater, we calculated the saturation index (SI) for fluorite, defined as, SI = log (IAP / Ksp), where IAP is the ion-activity product of the dissolved mineral constituents and Ksp is the mineral solubility product. By convention, a value of SI < 0 denotes undersaturation favouring mineral dissolution, SI = 0 indicates equilibrium with no dissolution, and SI > 0 reflects supersaturation favouring mineral precipitation. The calculated SI values for fluorite and synchysite in groundwater are negative (groundwater data from[11], calculation based on PHREEQC). The crystal morphologies and internal textures of fluorite and synchysite further enhance their susceptibility to dissolution under supergene weathering. Fluorite (especially Flr-II) is pervasively fractured and porous, and synchysite forms lath-shaped crystals (Fig. 3a,b). These features generate high specific surface areas, promoting mineral–water interaction and dissolution[28,29].

Extreme magmatic fractionation primes bedrocks for regolith-hosted HREE deposits

The Early Cretaceous syenogranite and its coexisting monzogranite within the Shitouping deposit area (Extended Data Fig. 2) exhibit indistinguishable zircon U–Pb ages, zircon Hf isotopic compositions [$\varepsilon Hf_{(t)}$ = -4.4 to +1.2], and whole-rock Nd isotopes [$\varepsilon Nd_{(t)}$ = -4.5 to -3.4], indicating derivation from partial melting of a common crustal source[20]. The HREE-enriched syenogranite, which is the bedrock of the regolith-hosted HREE saprolite ores, exhibits a higher degree of fractionation, evidenced by

elevated whole-rock Rb/Sr ratios[30] (Fig. 5a) and strong Eu anomalies[31] (Fig. 5b). These features suggest that the HREE enrichment of the Shitouping syenogranite is governed primarily by fractional crystallization.

A high degree of fractionation is further recorded by a distinctive trace-element fingerprint, characterized by pronounced depletion in P (< ~70 ppm; Fig. 5c), Ti (< ~500 ppm; Fig. 5d), and enrichment in F (Extended Data Table 1). This coupled P–Ti depletion and F enrichment is evident not only in the Shitouping bedrock but also in the bedrock of nearby regolith-hosted HREE deposits (e.g., Zudong and Dabu) and in the bedrock (HM granite) of a regolith-hosted HREE occurrence in Myanmar[32]. The pattern is consistent with early crystallization of major P- and Ti-bearing phases—apatite and Fe–Ti oxides (magnetite and ilmenite)—which progressively sequester these elements and deplete the residual melt. Consequently, refractory HREE-hosting minerals such as xenotime and titanite become exceedingly scarce in highly fractionated granites[33,34]. Despite their high mineral/melt partition coefficients for HREE[33–36], their minute modal abundances (Fig. 5c,d) limit them to sequestering only a negligible fraction of the bulk HREE budget. Progressive melt fractionation, conversely, enriches fluorine in the residual melt and promotes fluorite crystallization[12,37]. The favorable substitution of HREE, relative to LREE, for Ca results in high fluorite/melt partition coefficients and the preferential enrichment of HREE (notably Gd and Y) in igneous fluorite[38].

Targeting F-rich and P–Ti poor granites

Highly fractionated granites are globally widespread. When such intrusions possess HREE mineral assemblages comparable to the Shitouping syenogranite and undergo weathering under warm, humid conditions (Fig. 1), they can produce regolith-hosted HREE deposits. We propose that the formation of such deposits requires a bedrock that is enriched in labile HREE-bearing minerals, particularly fluorite, which is common in highly fractionated granites, while being depleted in refractory HREE-bearing minerals such as xenotime and titanite. Therefore, exploration for regolith-hosted HREE deposits should prioritize highly fractionated granites enriched in fluorine and depleted in

phosphorus and titanium.

Figures

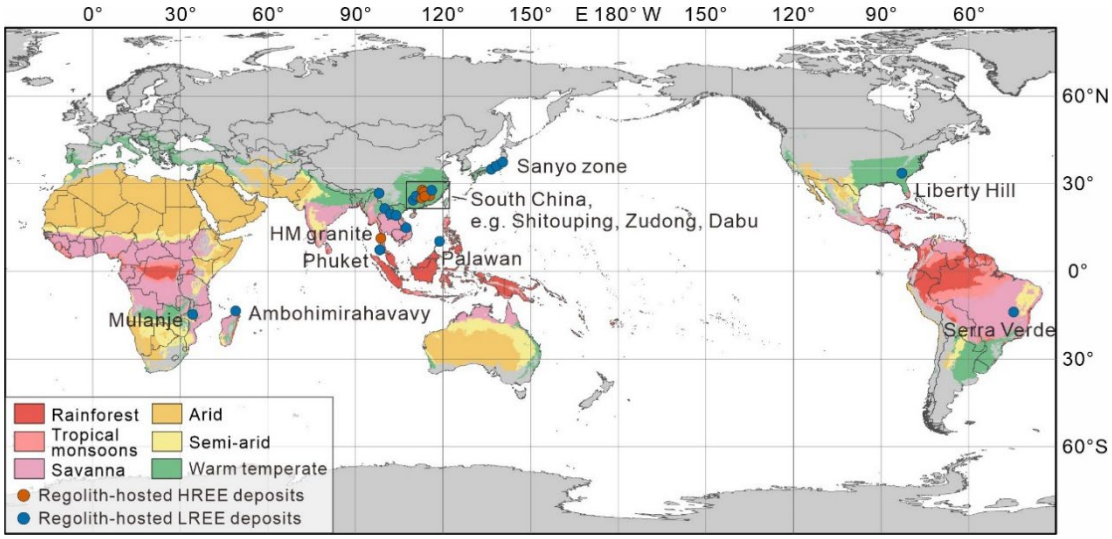


Fig. 1 | Global distribution of regolith-hosted REE deposits. Deposit locations were compiled from South China[8,39], Southeast Asia[40], Sanyo zone[41], HM granite[32], Phuket[42], Palawan[43], Liberty Hill[44], Serra Verde[45], Mulanje[46], and Ambohimirahavavy[47]. Climate distribution modified after the Köppen–Geiger climate zones[48].

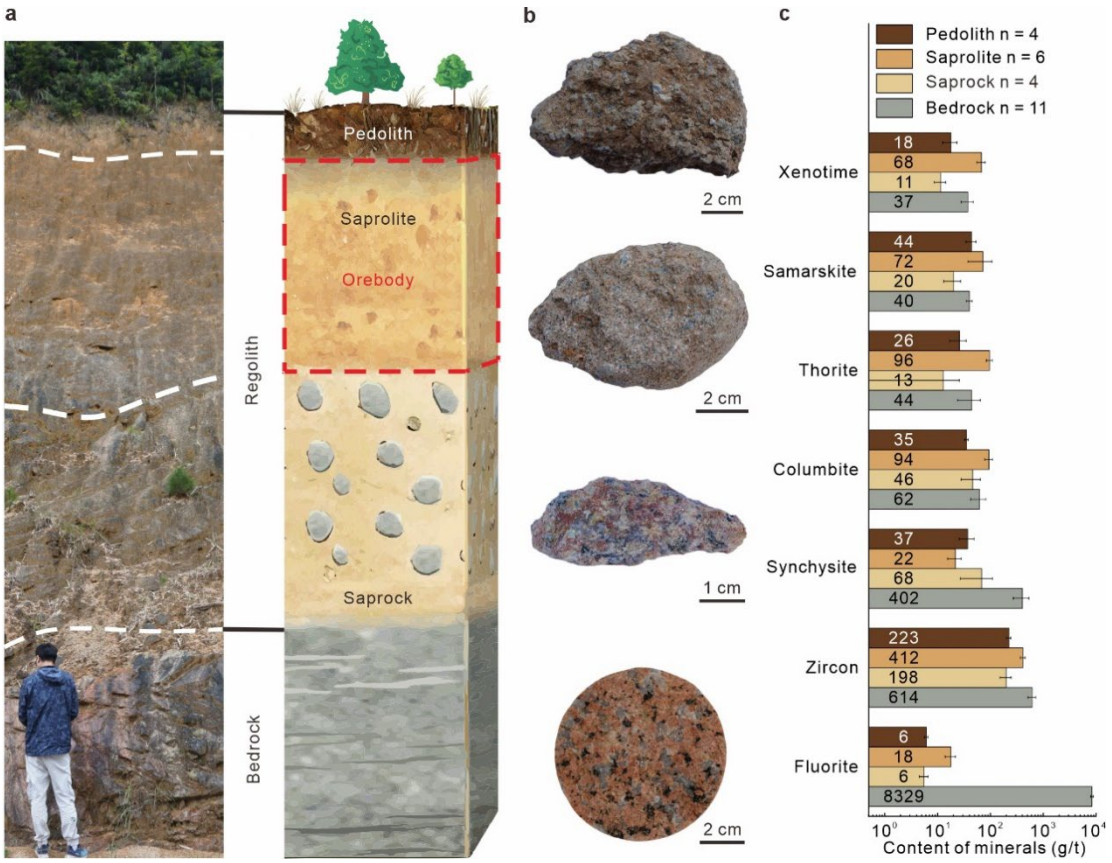
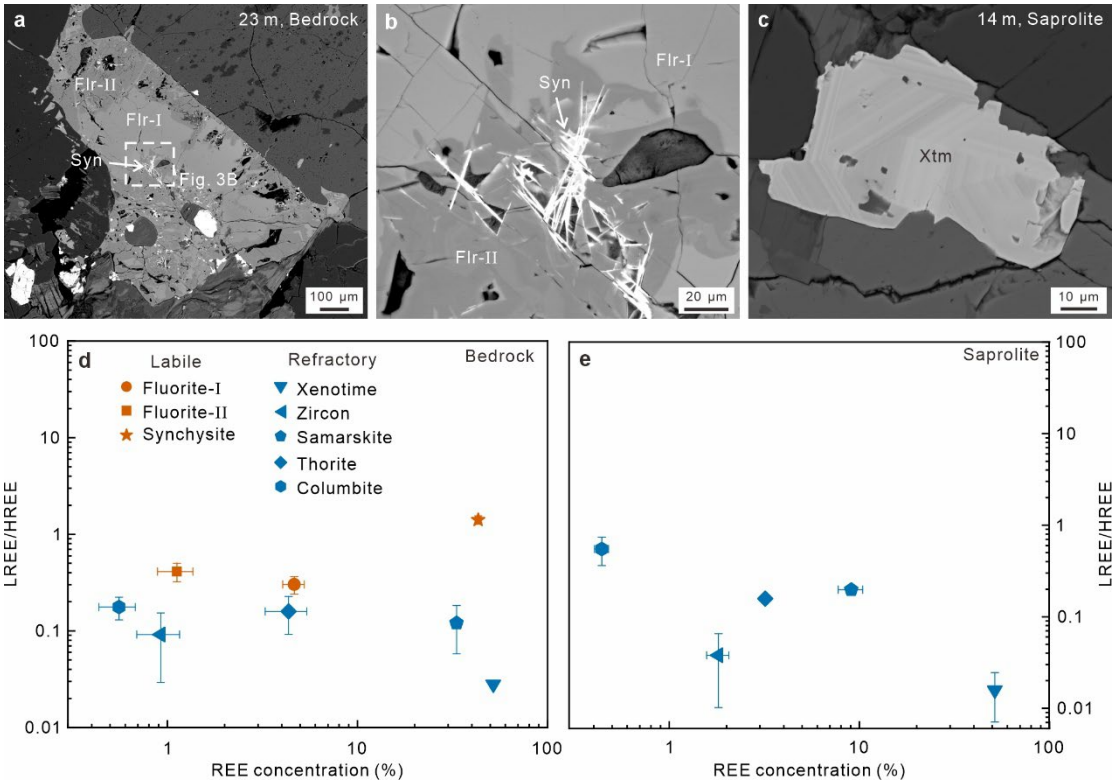
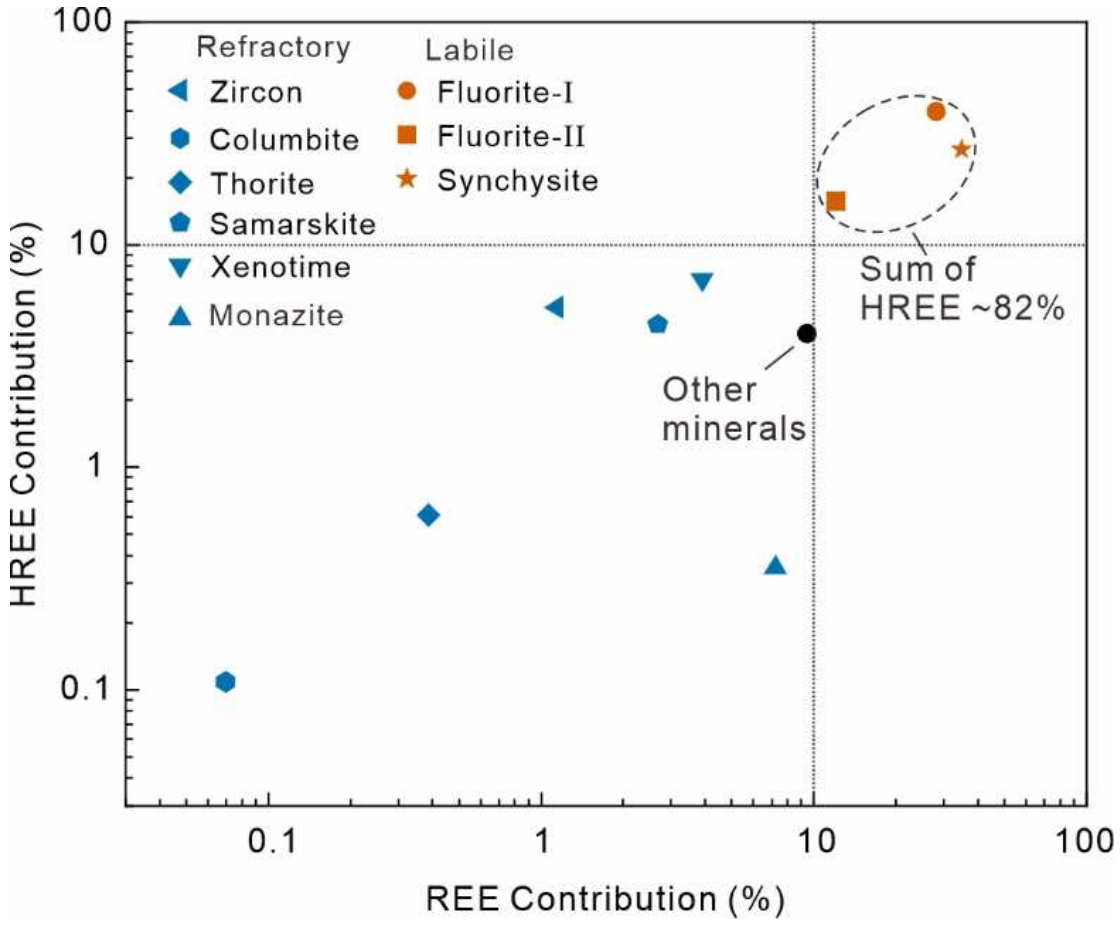


Fig. 2 | Weathering profile of the Shitouping regolith-hosted HREE deposit, Nanling Region, South China. a, Typical weathering profile, comprising surficial regolith and underlying bedrock. **b**, Photographs of representative samples from each weathering horizon. **c**, Abundances of REE-bearing minerals across the different weathering horizons. Mineral abundances are reported as mass fractions, converted from TIMA-derived modal volumes. Mass fractions were calculated by multiplying each mineral's volume percent by its density and then normalizing to 100%.



196

197 **Fig. 3 | Petrographic observations and REE contents of samples from different**
198 **weathering horizons. a**,**b**, Fluorite and synchysite in the fresh bedrock. **c**, Sample from
199 saprolite, fluorite and synchysite are rarely observed, xenotime largely preserves its
200 primary crystal shape and zoning. **d**,**e**, Concentration of REE in minerals of the bedrock
201 and saprolite. Abbreviations: Flr, fluorite; Syn, synchysite; Xtm, xenotime.



202

203 **Fig. 4 | Contribution of different minerals to REE and HREE contents of the**

204 **bedrock.** "Other minerals" refer to REE-bearing minerals such as apatite and titanite.

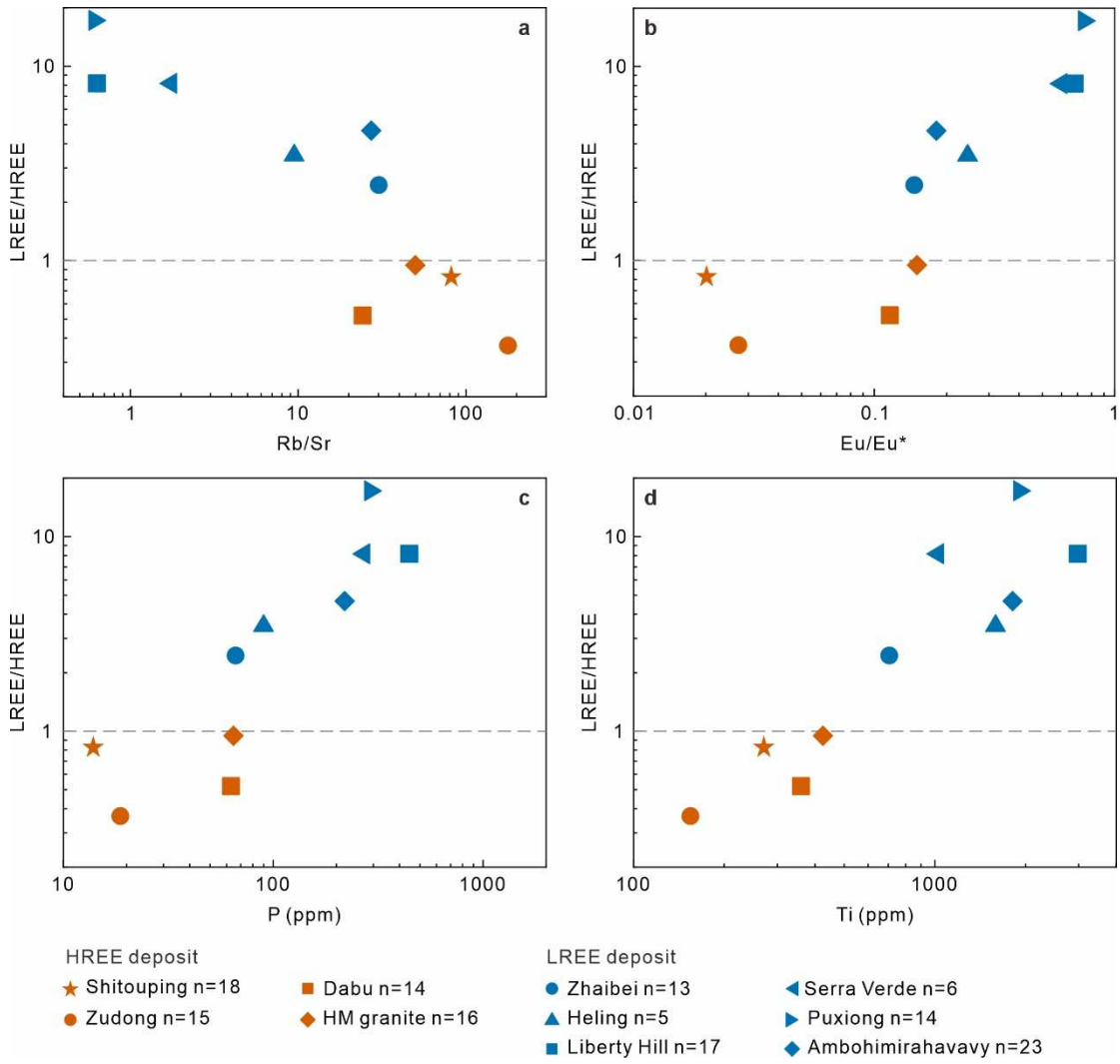


Fig. 5 | Comparison of bedrock geochemical parameters between representative regolith-hosted HREE deposits and LREE deposits. a,**b**, The data show that increasing magmatic crystallization fractionation—higher Rb/Sr and negative Eu anomalies [Eu/Eu*, chondrite normalized Eu/(Sm × Gd)$^{1/2}$]—is associated with decreasing LREE/HREE ratios and concomitant declines in P (**c**) and Ti (**d**) contents. Data for Shitouping, Zudong, Dabu, Zhaibei, and Heling are from this study. Comparative data are sourced from: HM granite[32], Liberty Hill[44], Serra Verde[49], Puxiong[50], and Ambohimirahavavy[47].

References

1. Hatch, G. P. Dynamics in the global market for rare earths. *Elements* **8**, 341–346 (2012). doi:10.2113/gselements.8.5.341.
2. Cheisson, T. & Schelter, E. J. Rare earth elements: Mendeleev's bane, modern marvels. *Science* **363**, 489–493 (2019). doi:10.1126/science.aau7628.
3. Xu, C., Kynický, J., Smith, M. P., Kopriva, A., Brtnický, M., Urubek, T., Yang, Y., Zhao, Z., He, C. & Song, W. L. Origin of heavy rare earth mineralization in South China. *Nat. Commun.* **8**, 14598 (2017). doi:10.1038/ncomms14598.
4. Borst, A. M., Smith, M. P., Finch, A. A., Estrade, G., Villanova-de-Benavent, C., Nason, P., Marquis, E., Horsburgh, N. J., Goodenough, K. M., Xu, C., Kynický, J. & Geraki, K. Adsorption of rare earth elements in regolith-hosted clay deposits. *Nat. Commun.* **11**, 4386 (2020). doi:10.1038/s41467-020-17801-5.
5. Strzelecki, A. C., Migdisov, A., Boukhalfa, H., Sauer, K., McIntosh, K. G., Currier, R. P., Williams-Jones, A. E. & Guo, X. Fluocerite as a precursor to rare earth element fractionation in ore-forming systems. *Nat. Geosci.* **15**, 327–333 (2022). doi:10.1038/s41561-022-00921-6.
6. U.S. Geological Survey. *Mineral commodity summaries 2022* (U.S. Geological Survey, 2002). doi:10.3133/mcs2022.
7. Li, M. Y. H. & Zhou, M. F. The role of clay minerals in formation of the regolith-hosted heavy rare earth element deposits. *Am. Mineral.* **105**, 92–108 (2020). doi:10.2138/am-2020-7061.
8. Sanematsu, K. & Watanabe, Y. Characteristics and genesis of ion adsorption-type rare earth element deposits. *Rev. Econ. Geol.* **18**, 55–79 (2016). doi:10.5382/Rev.18.03.
9. Li, M. Y. H. & Zhou, M. F. Hyper-enrichment of heavy rare earth elements in highly evolved granites through multiple hydrothermal mobilizations. *Am. Mineral.* **109**, 1945–1959 (2024). doi:10.2138/am-2023-9117.
10. Shi, A. G., Xu, C., Fan, C. X., Chakhmouradian, A. R., Brenna, M. & Wei, C. W. Structural defects of heavy rare earth element minerals in granite accelerate their

decomposition and facilitate mineralization during weathering. *Econ. Geol.* **119**, 871–883 (2024). doi:10.5382/econgeo.5057.

11. Li, M. Y. H., Kwong, H. T., Williams-Jones, A. E. & Zhou, M. F. The thermodynamics of rare earth element liberation, mobilization and supergene enrichment during groundwater-regolith interaction. *Geochim. Cosmochim. Acta* **330**, 258–277 (2022). doi:10.1016/j.gca.2021.05.002.
12. Price, J. D., Hogan, J. P., Gilbert, M. C., London, D. & Morgan, G. B. Experimental study of titanite-fluorite equilibria in the A-type Mount Scott Granite: Implications for assessing F contents of felsic magma. *Geology* **27**, 951 (1999). doi:10.1130/0091-7613(1999)027<0951:ESOTFE>2.3.CO;2.
13. Bucher, K. & Seelig, U. Bristen granite: a highly differentiated, fluorite-bearing A-type granite from the Aar massif, Central Alps, Switzerland. *Swiss J. Geosci.* **111**, 317–340 (2018). doi:10.1007/s00015-017-0294-z.
14. Huang, D. H., Wu, C. Y. & Han, J. Z. REE geochemistry and mineralization characteristics of the Zudong and Guanxi granites, Jiangxi province. *Acta Geol. Sin.* **2**, 139–157 (1989). doi:10.1111/j.1755-6724.1989.mp2002004.x.
15. Li, M. Y. H., Zhou, M. F. & Williams-Jones, A. E. The genesis of regolith-hosted heavy rare earth element deposits: Insights from the world-class Zudong deposit in Jiangxi province, south China. *Econ. Geol.* **114**, 541–568 (2019). doi:10.5382/econgeo.4642.
16. Wang, H., He, H. P., Yang, W. B., Bao, Z. W., Liang, X. L., Zhu, J. X., Ma, L. Y. & Huang, Y. F. Zircon texture and composition fingerprint HREE enrichment in muscovite granite bedrock of the Dabu ion-adsorption REE deposit, South China. *Chem. Geol.* **616**, 121231 (2023). doi:10.1016/j.chemgeo.2022.121231.
17. Bao, Z. W. & Zhao, Z. H. Geochemistry of mineralization with exchangeable REY in the weathering crusts of granitic rocks in South China. *Ore Geol. Rev.* **33**, 519–535 (2008). doi:10.1016/j.oregeorev.2007.03.005.
18. Fan, C. X., Xu, C., Shi, A. G., Smith, M. P., Kynicky, J. & Wei, C. W. Origin of heavy rare earth elements in highly fractionated peraluminous granites. *Geochim. Cosmochim. Acta* **343**, 371–383 (2023). doi:10.1016/j.gca.2022.12.019.

19. Beard, C. D., Marquis, E., Smith, M. P., Li, M. Y. H., Estrade, G. & Goodenough, K. M. Ion adsorption mineralisation in regolith-hosted REE deposits. in *Geology, Geochemistry and Formation of Supergene Mineral Deposits in Deeply Weathered Terrain* (eds Bowell, R. J. & Butt, C. R. M.) 365–394 (Springer Nature Switzerland, Cham, 2025). doi:10.1007/978-3-031-75733-4_14.
20. Cao, M. X., Wang, X. G., Zhang, D. F., Zhang, Y. W., Gong, L. X. & Zhong, W. Petrogenesis and REE mineralogical characteristics of Shitouping granites in southern Jiangxi province: Implication for HREE mineralization in South China. *Ore Geol. Rev.* **168**, 106011 (2024). doi:10.1016/j.oregeorev.2024.106011.
21. Singh, T., Upadhyay, D., Patel, A. K. & Mishra, B. High MREE-HREE solubility in a carbonatite-derived hydrothermal fluid: Evidence from fluorite-hosted fluid inclusions in the Amba Dongar carbonatite complex, India. *Chem. Geol.* **613**, 121162 (2022). doi:10.1016/j.chemgeo.2022.121162.
22. Möller, P., Parekh, P. P. & Schneider, H.-J. The application of Tb/Ca-Tb/La abundance ratios to problems of fluorspar genesis. *Miner. Deposita* **11**, 111–116 (1976). doi:10.1007/BF00203098.
23. Shannon, R. D. Revised effective ionic radii and systematic studies of interatomic distances in halides and chalcogenides. *Acta Crystallogr. Sect. A* **32**, 751–767 (1976). doi:10.1107/S0567739476001551.
24. Bau, M. & Dulski, P. Comparative study of yttrium and rare-earth element behaviours in fluorine-rich hydrothermal fluids. *Contrib. Mineral. Petrol.* **119**, 213 223 (1995). doi:10.1007/BF00307282.
25. Tsay, A., Zajacz, Z. & Sanchez-Valle, C. Efficient mobilization and fractionation of rare-earth elements by aqueous fluids upon slab dehydration. *Earth Planet. Sci. Lett.* **398**, 101–112 (2014). doi:10.1016/j.epsl.2014.04.042.
26. Zhang, R. H., Hu, S. M. & Zhang, X. T. Experimental study of dissolution rates of fluorite in HCl–H_2O solutions. *Aquat. Geochem.* **12**, 123–159 (2006). doi:10.1007/s10498-005-3658-3.
27. He, Y. L., Ma, L. Y., Liang, X. L., Li, X. R., Zhu, J. X. & He, H. P. Resistant rare earth phosphates as possible sources of environmental dissolved rare earth

303 elements: Insights from experimental bio-weathering of xenotime and monazite.
304 *Chem. Geol.* **661**, 122186 (2024). doi:10.1016/j.chemgeo.2024.122186.
305 28. Putnis, C. V. & Ruiz-Agudo, E. The mineral-water interface: Where minerals react
306 with the environment. *Elements* **9**, 177–182 (2013).
307 doi:10.2113/gselements.9.3.177.
308 29. Putnis, A. Why mineral interfaces matter. *Science* **343**, 1441–1442 (2014).
309 doi:10.1126/science.1250884.
310 30. Long, P. E. Experimental determination of partition coefficients for Rb, Sr and Ba
311 between alkali feldspar and silicate liquid. *Geochim. Cosmochim. Acta* **42**, 833–
312 846 (1978). doi:10.1016/0016-7037(78)90096-0.
313 31. Gelman, S. E., Deering, C. D., Bachmann, O., Huber, C. & Gutiérrez, F. J.
314 Identifying the crystal graveyards remaining after large silicic eruptions. *Earth*
315 *Planet. Sci. Lett.* **403**, 299–306 (2014). doi:10.1016/j.epsl.2014.07.005.
316 32. Sanematsu, K., Ejima, T., Kon, Y., Manaka, T., Zaw, K., Morita, S. & Seo, Y.
317 Fractionation of rare-earth elements during magmatic differentiation and
318 weathering of calc-alkaline granites in southern Myanmar. *Mineral. Mag.* **80**, 77–
319 102 (2016). doi:10.1180/minmag.2016.080.053.
320 33. Wark, D. A. & Miller, C. F. Accessory mineral behavior during differentiation of
321 a granite suite: monazite, xenotime and zircon in the Sweetwater Wash pluton,
322 southeastern California, U.S.A. *Chem. Geol.* **110**, 49–67 (1993).
323 doi:10.1016/0009-2541(93)90247-G.
324 34. Colombini, L. L., Miller, C. F., Gualda, G. A. R., Wooden, J. L. & Miller, J. S.
325 Sphene and zircon in the Highland Range volcanic sequence (Miocene, southern
326 Nevada, USA): elemental partitioning, phase relations, and influence on evolution
327 of silicic magma. *Mineral. Petrol.* **102**, 29–50 (2011). doi:10.1007/s00710-011-
328 0177-3.
329 35. Arth, J. Behavior of trace elements during magmatic processes - A summary of
330 theoretical models and their applications. *J. Res. US Geol. Surv.* **4**, 41–47 (1976).
331 36. Bea, F., Pereira, M. D. & Stroh, A. Mineral/leucosome trace-element partitioning
332 in a peraluminous migmatite (a laser ablation-ICP-MS study). *Chem. Geol.* **117**,

291–312 (1994). doi:10.1016/0009-2541(94)90133-3.

37. Audťat, A., Gñther, D. & Heinrich, C. A. Magmatic-hydrothermal evolution in a fractionating granite: a microchemical study of the Sn-W-F-mineralized mole granite (Australia). *Geochim. Cosmochim. Acta* **64**, 3373–3393 (2000). doi:10.1016/S0016-7037(00)00428-2.

38. Veksler, I. V., Dorfman, A. M., Kamenetsky, M., Dulski, P. & Dingwell, D. B. Partitioning of lanthanides and Y between immiscible silicate and fluoride melts, fluorite and cryolite and the origin of the lanthanide tetrad effect in igneous rocks. *Geochim. Cosmochim. Acta* **69**, 2847–2860 (2005). doi:10.1016/j.gca.2004.08.007.

39. Li, Y. H. M., Zhao, W. W. & Zhou, M. F. Nature of parent rocks, mineralization styles and ore genesis of regolith-hosted REE deposits in South China: An integrated genetic model. *J. Asian Earth Sci.* **148**, 65–95 (2017). doi:10.1016/j.jseaes.2017.08.004.

40. Sanematsu, K., Murakami, H., Watanabe, Y., Duangsurigna, S. & Siphandone, V. Enrichment of rare earth elements (REE) in granitic rocks and their weathered crusts in central and southern Laos. *Bull. Geol. Surv. Jpn.* **60**, 527–558 (2009). doi:10.9795/bullgsj.60.527.

41. Watanabe, Y., Kon, Y., Echigo, T. & Kamei, A. Differential fractionation of rare earth elements in oxidized and reduced granitic rocks: Implication for heavy rare earth enriched ion adsorption mineralization. *Resour. Geol.* **67**, 35–52 (2017). doi:10.1111/rge.12119.

42. Sanematsu, K., Kon, Y., Imai, A., Watanabe, K. & Watanabe, Y. Geochemical and mineralogical characteristics of ion-adsorption type REE mineralization in Phuket, Thailand. *Miner. Deposita* **48**, 437–451 (2013). doi:10.1007/s00126-011-0380-5.

43. Padrones, J. T., Imai, A. & Takahashi, R. Geochemical behavior of rare earth elements in weathered granitic rocks in northern Palawan, Philippines. *Resour. Geol.* **67**, 231–253 (2017). doi:10.1111/rge.12123.

44. Bern, C. R., Yesavage, T. & Foley, N. K. Ion-adsorption REEs in regolith of the Liberty Hill pluton, South Carolina, USA: An effect of hydrothermal alteration. *J.*

Geochem. Explor. **172**, 29–40 (2017). doi:10.1016/j.gexplo.2016.09.009.

45. Santana, I. V. & Botelho, N. F. REE residence, behaviour and recovery from a weathering profile related to the Serra Dourada Granite, Goiás/Tocantins States, Brazil. *Ore Geol. Rev.* **143**, 104751 (2022). doi:10.1016/j.oregeorev.2022.104751.
46. Platt, R. G., Wall, F., Williams, C. T. & Woolley, A. R. Zirconolite, chevkinite and other rare earth minerals from nepheline syenites and peralkaline granites and syenites of the Chilwa Alkaline Province, Malawi. *Mineral. Mag.* **51**, 253–263 (1987). doi:10.1180/minmag.1987.051.360.07.
47. Estrade, G., Béziat, D., Salvi, S., Tiepolo, M., Paquette, J.-L. & Rakotovao, S. Unusual evolution of silica-under- and -oversaturated alkaline rocks in the Cenozoic Ambohimirahavavy Complex (Madagascar): Mineralogical and geochemical evidence. *Lithos* **206–207**, 361–383 (2014). doi:10.1016/j.lithos.2014.08.008.
48. Beck, H. E., Zimmermann, N. E., McVicar, T. R., Vergopolan, N., Berg, A. & Wood, E. F. Present and future Köppen-Geiger climate classification maps at 1-km resolution. *Sci. Data* **5**, 180214 (2018). doi:10.1038/sdata.2018.214.
49. Feio, G. R. L. & Dall'Agnol, R. Geochemistry and petrogenesis of the Mesoarchean granites from the Canaã dos Carajás area, Carajás Province, Brazil: Implications for the origin of Archean granites. *Lithos* **154**, 33–52 (2012). doi:10.1016/j.lithos.2012.06.022.
50. Cheng, Y. B., Mao, J. W. & Spandler, C. Petrogenesis and geodynamic implications of the Gejiu igneous complex in the western Cathaysia block, South China. *Lithos* **175–176**, 213–229 (2013). doi:10.1016/j.lithos.2013.04.002.
51. Zhao, Z., Wang, D. H., Bagas, L. & Chen, Z. Y. Geochemical and REE mineralogical characteristics of the Zhaibei granite in Jiangxi province, southern China, and a model for the genesis of ion-adsorption REE deposits. *Ore Geol. Rev.* **140**, 104579 (2022). doi:10.1016/j.oregeorev.2021.104579.
52. Wang, M., Hei Li, M. Y., Zhou, M. F., Zhou, J. X., Sun, G., Zhou, Y. & Li, Y. Enrichment of rare earth elements during the weathering of alkaline igneous systems: Insights from the Puxiong regolith-hosted rare earth element deposit, SW

China. *Econ. Geol.* **119**, 161–187 (2024). doi:10.5382/econgeo.5024.

53. Zhao, X., Li, N. B., Smith, M. P., Tan, S. C., Fu, R. X., Yang, Y. Y. & Niu, H. C. Progressive enrichment of rare earth elements (REE) between parent granites and weathering crust contributed to the generation of regolith-hosted REE deposits in South China. *Geol. Soc. Am. Bull.* **137**, 4516–4532 (2025). doi:10.1130/B38051.1.
54. Mao, J. W., Zheng, W., Xie, G. Q., Lehmann, B. & Goldfarb, R. Recognition of a Middle–Late Jurassic arc-related porphyry copper belt along the southeast China coast: Geological characteristics and metallogenic implications. *Geology* **49**, 592–596 (2021). doi:10.1130/G48615.1.
55. Sun, S. -s. & McDonough, W. F. Chemical and isotopic systematics of oceanic basalts: implications for mantle composition and processes. *Geol. Soc. Lond. Spec. Publ.* **42**, 313–345 (1989). doi:10.1144/GSL.SP.1989.042.01.19.
56. Xie, Y. L., Verplanck, P. L., Hou, Z. Q. & Zhong, R. C. Chapter 12 Rare earth element deposits in China: A review and new understandings. *Rev. Econ. Geol.* **22**, 509–552 (2019). doi:10.5382/SP.22.12.
57. Wang, L. Z., Xu, C., Zhao, Z., Song, W. L. & Kynicky, J. Petrological and geochemical characteristics of Zhaibei granites in Nanling region, Southeast China: Implications for REE mineralization. *Ore Geol. Rev.* **64**, 569–582 (2015). doi:10.1016/j.oregeorev.2014.04.004.
58. Estrade, G., Marquis, E., Smith, M., Goodenough, K. & Nason, P. REE concentration processes in ion adsorption deposits: Evidence from the Ambohimirahavavy alkaline complex in Madagascar. *Ore Geol. Rev.* **112**, 103027 (2019). doi:10.1016/j.oregeorev.2019.103027.

Methods

Sample collection from representative deposits

Bedrock samples were collected from deep drill cores, quarries, and in the vicinity of large engineering excavations (e.g., bridges and tunnels) to ensure sample freshness. A total of 65 fresh bedrock samples were collected from the Shitouping, Zudong, Dabu, Zhaibei, and Heling areas (Supplementary Table 1). The principal study area was syenogranite from the Shitouping regolith-hosted HREE deposit (Sample No. 008-2, 036-1, 042-1, 042-2, 060-3, 067-1, 067-2, 067-3, 069-2, 077-2, 077-3, 087-1, 087-3, 097-1, 097-2, 108-1, 108-3, and 128-1) (Extended Data Fig. 2). In addition, we conducted field investigations and collected samples from other representative regolith-hosted REE deposits in South China for geochemical comparison. The selected areas and lithologies include: Zudong regolith-hosted HREE deposit[15]—medium-grained alkaline granite (Sample No. 24ZD-1, 24ZD-7, 24ZD-10, 24ZD-12, 24ZD-13, 24ZD-21, 24ZD-32, 24ZD-33, ZD-3, ZD-19, ZD-26, ZD-31, ZK005-22, and ZK20-10) and medium-grained biotite granite (Sample No. ZD-10) (Extended Data Fig. 8); Dabu regolith-hosted HREE deposit[16]—muscovite granites (Sample No. 24DB-3, 24DB-4, 24DB-8, 24DB-12, 24DB-13, 24DB-18, ZK22033-1, ZK23021-3, ZK23013-3, ZK23061-3, ZK23148-2, and ZK23159-2) and biotite monzogranites (Sample No. ZK23116-2 and ZK23178-3) (Extended Data Fig. 9); Zhaibei regolith-hosted LREE deposit[51]—biotite syenogranite (Sample No. 24ZB-1 to 24ZB-4, 24ZB-6, 24ZB-10, 24ZB-14, ZK14-11, ZK15-21, ZBB-3, ZK13-11, and ZKS28-1) and muscovitic alkali-feldspar granite (Sample No. ZKS29-2) (Extended Data Fig. 10); and Heling regolith-hosted LREE deposit[17]—granitic porphyry (Sample No. 24HL-8) and rhyolitic tuff (Sample No. 24HL-2, 24HL-3, 24HL-5, and 24HL-11) (Extended Data Fig. 11). In Shitouping drill cores collected 4 saprock samples (No. 035-H21, 046-H19, 046-H20 and 139-H13, 11–19 m in depth), 6 saprolite samples (No. 025-H6, 025-H12, 025-H13, 025-H17, 046-H10 and 095-H11, 5–16 m in depth), and 4 pedolith samples (No. 062-H1, 062-H2, 062-H3 and 139-H1, 0.5–2 m in depth).

445

446 Whole-rock trace element analysis

447 Pulverized samples were digested in a sealed Teflon beaker with ultrapure HF and
448 HNO_3 at 100 °C for four days. Elemental concentrations were measured using
449 inductively coupled plasma mass spectrometry (ICP-MS). Full analytical results are
450 provided in Supplementary Tables 1 and 2.

451

452 Scanning electron microscope analysis

453 Petrographic observations were conducted by scanning electron microscopy (SEM) on
454 a FEI NOVA NanoSEM fitted with an Oxford X-Max 50 detector. Analyses were
455 carried out at an accelerating voltage of 20 kV on carbon-coated specimens. The system
456 was equipped with an Oxford energy dispersive spectrometer (EDS) to enable rapid
457 semi quantitative elemental mapping of REE bearing phases. For both fluorite
458 morphotypes, imaging parameters were optimized with contrast set above 50 and
459 brightness above 35.

460 Mineralogical analyses were carried out on 25 representative carbon-coated thin
461 sections using a TESCAN Integrated Mineral Analyzer (TIMA). Detailed results
462 presented in Supplementary Table 3. Measurements were conducted on a MIRA3
463 scanning electron microscope at an accelerating voltage of 25 kV, a probe current of
464 8.24 nA, and a working distance of 15 mm, employing a pixel spacing of 3 μm and dot
465 spacing of 9 μm. Beam current and backscatter electron (BSE) signal intensities were
466 automatically calibrated via a platinum Faraday cup, and EDS performance was
467 validated using a manganese standard. Data acquisition utilized the TIMA liberation
468 analysis module. An additional EDS parameter — Ce content — served to discriminate
469 two distinct fluorite populations in the bedrock, owing to their markedly different Ce
470 concentrations (Extended Data Fig. 6), with comparative imagery shown in Extended
471 Data Fig. 12.

472

473 Electron probe microanalysis

474 REE concentrations in REE-bearing minerals were determined by electron probe

475 microanalysis (EPMA), using a JEOL JXA-8230 microanalyzer operated at 15 kV
476 accelerating voltage and 5 nA beam current. Beam diameter was adjusted to 3–5 μm to
477 match grain sizes, yielding individual REE detection limits of approximately 300 ppm.
478 All measurements were corrected via the ZAF procedure, and the corrected data are
479 presented in Supplementary Tables 4 and 5.
480 Electron probe mapping was employed to delineate compositional zoning in
481 fluorite (Extended Data Fig. 6). Analyses were conducted at 20 kV with a 1 μm beam
482 spot and a 300 × 300-pixel acquisition grid to ensure high spatial resolution. The
483 scanning area and resolution were adapted to the dimensions of individual mineral
484 grains.
485
486 Mass balance calculations
487 Mass balance calculations were performed to quantify the contribution of fluid during
488 the alteration of Flr-I to Flr-II and synchysite to the enrichment of REE. These
489 calculations are based on petrographic evidence showing that Flr-I exhibits a magmatic
490 origin, whereas Flr-II and synchysite pseudomorphically replace Flr-I. Assuming
491 isovolumetric alteration of Flr-I to Flr-II with concomitant formation of an extra volume
492 of synchysite, REE abundance in each mineral was expressed as ωREE (ppm), defined
493 as the mineral's mass fraction (%) multiplied by its REE concentration (ppm)[52,53].
494 Accordingly, the pre-alteration ωREE of Flr-II (ωREE pre-altered Flr-II) was calculated
495 by multiplying the mass of Flr-II by the REE concentration of Flr-I. 20 fluorite grains
496 were analyzed (Extended Data Fig. 13), and the results are summarized in
497 Supplementary Table 6. The mean ωREE pre-altered Flr-II is ~237,517 ppm, which
498 closely matches the sum of the measured ωREE values for Flr-II and synchysite
499 (57,389 ppm + 168,879 ppm). This concordance demonstrates that the REE in Flr-II
500 and synchysite derive from Flr-I. Finally, mineral ωREE values (e.g. ωREE Flr =
501 fluorite's mass fraction × fluorite's REE concentration) were compared to whole-rock
502 REE content to quantify the contribution of REE-bearing minerals to the whole-rock
503 REE content of the Shitouping deposit is presented in Fig. 4, with full data listed in
504 Supplementary Table 7.

femtosecond-LA-ICP-MS analysis

In-situ trace element analyses of fluorite were performed with a J200 Tandem XQ femtosecond (fs) laser-ablation system (Applied Spectra) coupled to a Thermo Scientific iCap-RQ inductively coupled plasma mass spectrometer (ICP-MS). Helium was used as the carrier gas and argon as the make-up gas. Single-spot analyses comprised 105 seconds (s) total acquisition time (20 s background, 45 s ablation, 40 s wash/washout), whereas line scans used a 120 s protocol (20 s background, 55 s continuous ablation, 50 s wash). Line scans employed a 40 μm spot and 60 μm track length at 1.0 J cm^{-2} and 6 Hz. The National Institute of Standards and Technology (NIST) standard reference material (SRM) 610 served as the external standard, and Ca was used as the internal standard to correct trace-element abundances. Reference materials (Columbia River Basalt BCR-2G, NIST SRM 610, NIST SRM 612 and Hawaii Volcano Observatory Basalt BHVO-2G) were analyzed as quality controls, with one standard run after every eight samples. Data reduction was performed in ICPMSDataCal v12.2 using the internal-standard approach; internal standard elements were chosen according to mineral phase (here, EPMA-measured Ca was used). Locations of the fluorite analysis points are reported in Extended Data Fig. 14 and Supplementary Table 8.

Acknowledgments: This project was funded by the National Natural Science Foundation of China (Grant 42472119), the National Science and Technology Major Project (Grant 2024ZD1001900), the Geological Exploration Project of Jiangxi province Finance (Grant 20220014), the Open Fund of MNR Key Laboratory of Ionic Rare Earth Resources and Environment (Grant 2022IRERE107). We thank D. F. Zhang and M. X. Cao for the field of geological investigations. We thank T. Ma and B. F. Chen for collecting information. We also thank helpful discussions with J. Z. Zuo, G. Chen and W. Zheng on granite formation.

Author contributions:

Conceptualization: S.D.Z., W.J. and J.W.M.

Methodology: S.D.Z., B.L., N.C., S.W.S., X.Y.M. and A.C.S.

Investigation: S.D.Z., X.G.W., L.X.G. and G.G.R.

Funding acquisition: W.J. and J.W.M.

Project administration: W.J. and M.L.

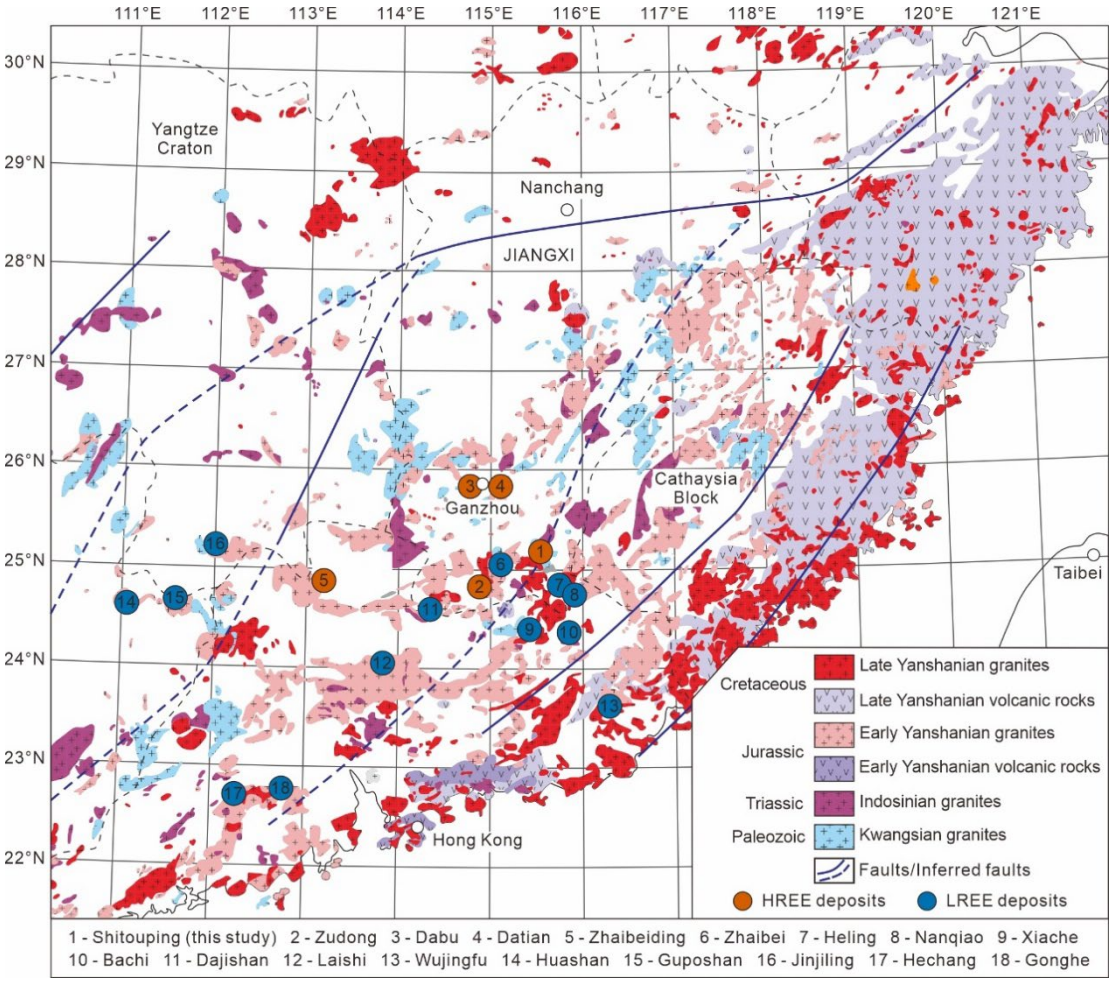
Writing – original draft: S.D.Z., W.J., J.W.M. and N.C.

Writing – review & editing: J.W.M., B.L. and A.C.S.

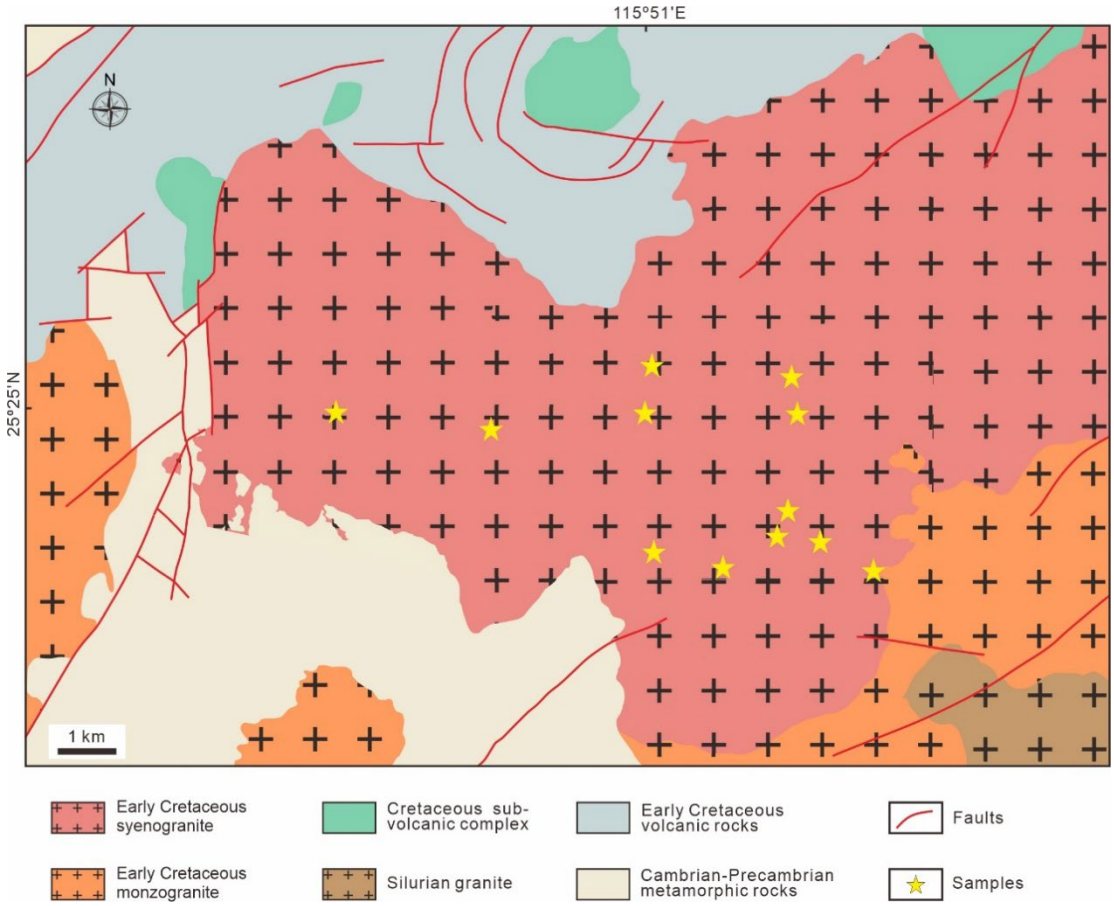
Competing interests: The authors declare that they have no competing interests.

Data and materials availability: All data are available in the main text or the supplementary materials.

Extended Data Figures and table



Extended Data Fig. 1 | Geological map of South China illustrating the distribution of major regolith-hosted REE deposits. Modified from[8,54], deposit locations from[8,20,39].

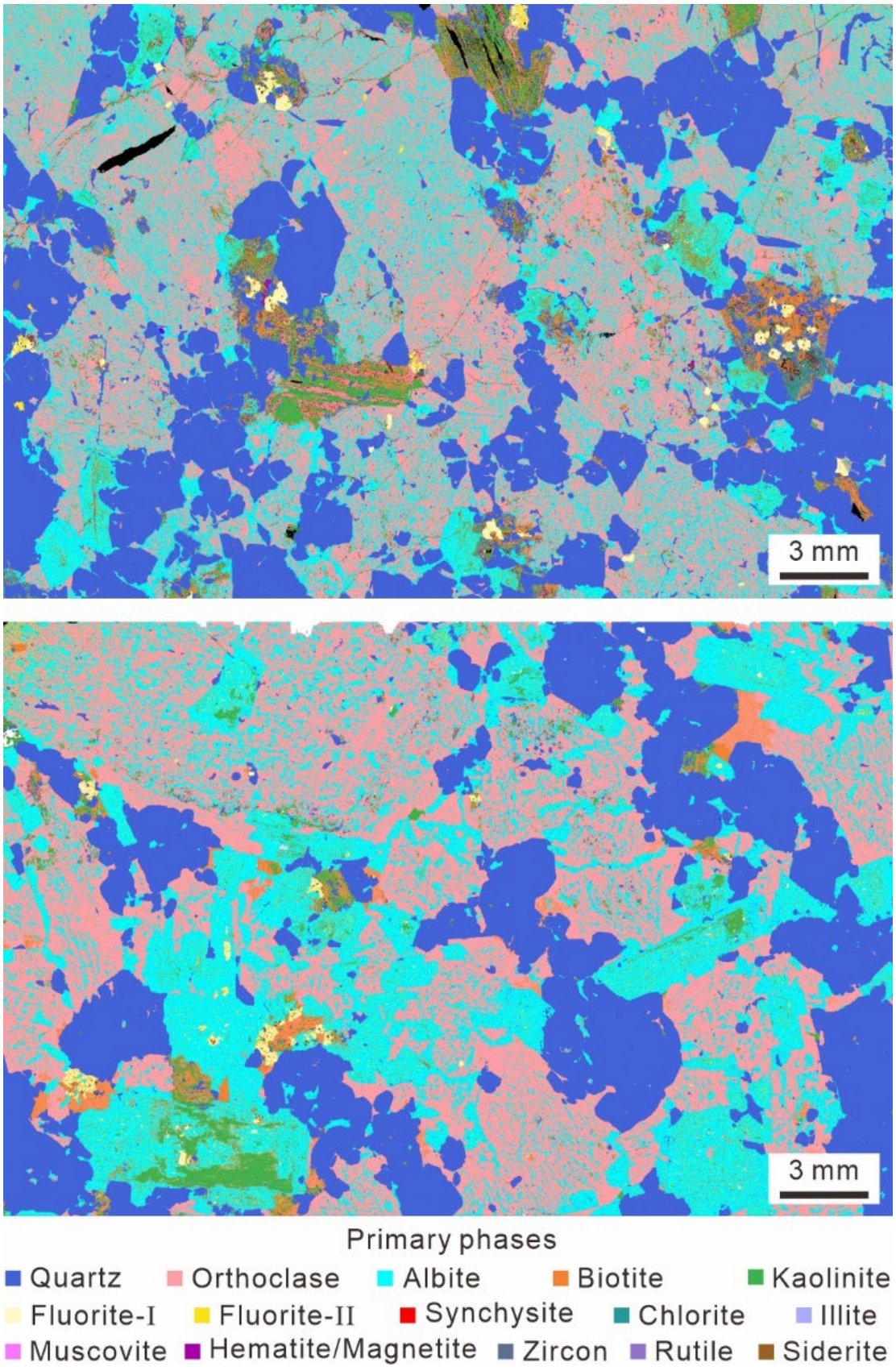


551

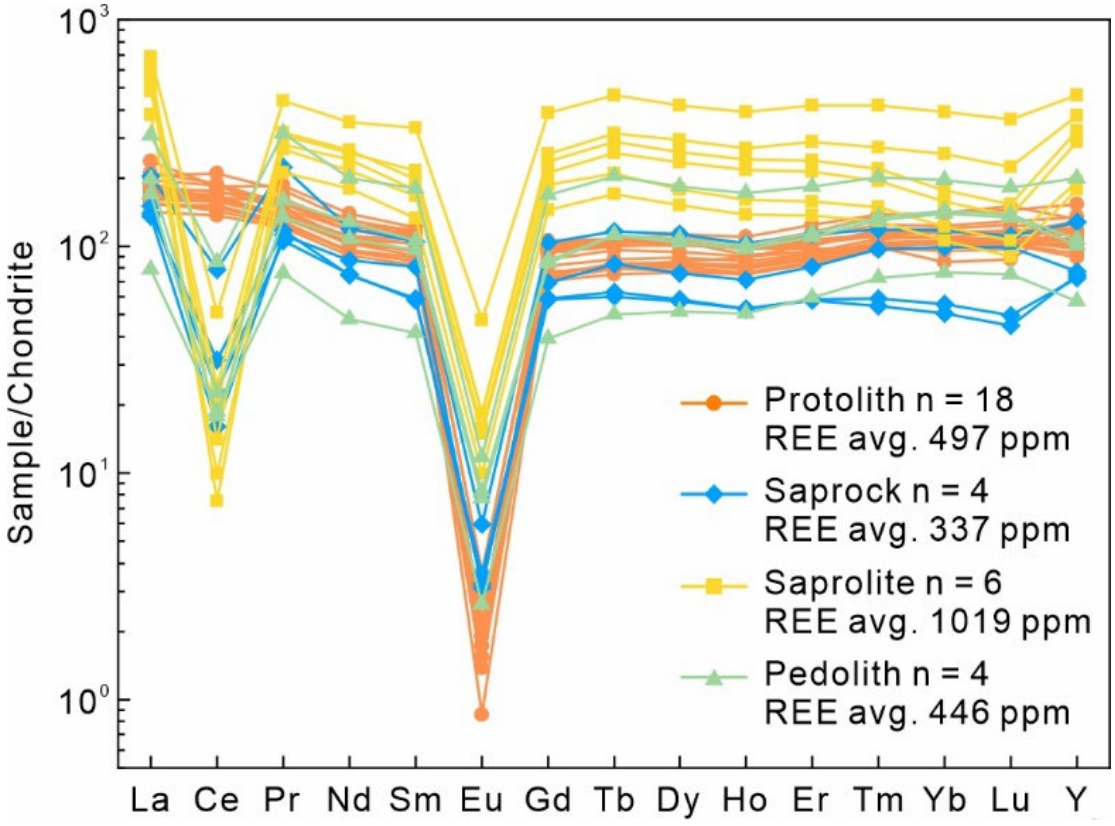
552 **Extended Data Fig. 2 | Simplified geological map of the Shitouping regolith-hosted**

553 **HREE deposit.** The regolith-hosted HREE ore bodies overlie the Early Cretaceous

554 syenogranite.



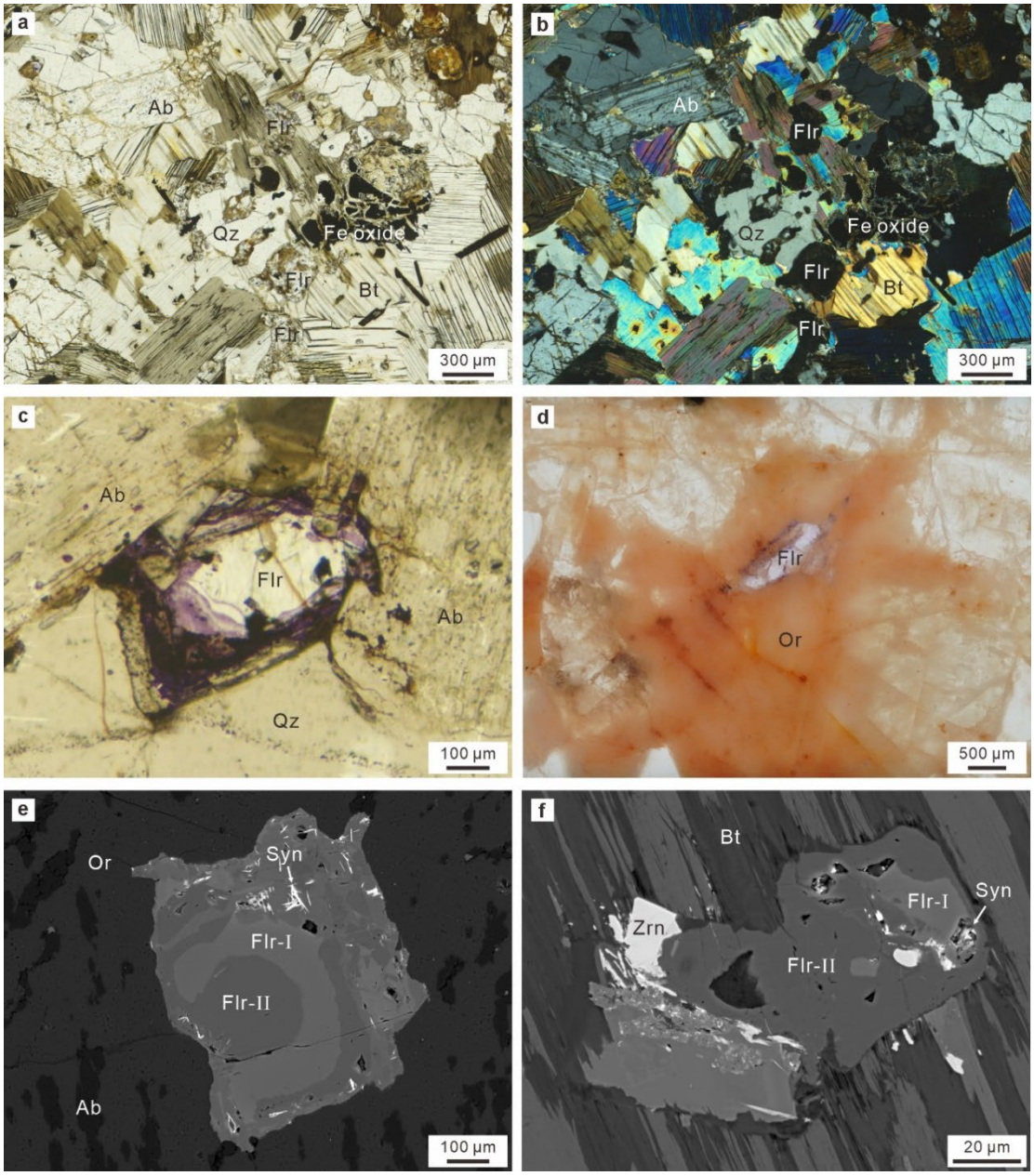
Extended Data Fig. 3 | Mineralogy and texture of the syenogranite bedrock by TESCAN Integrated Mineral Analyzer (TIMA) imaging.



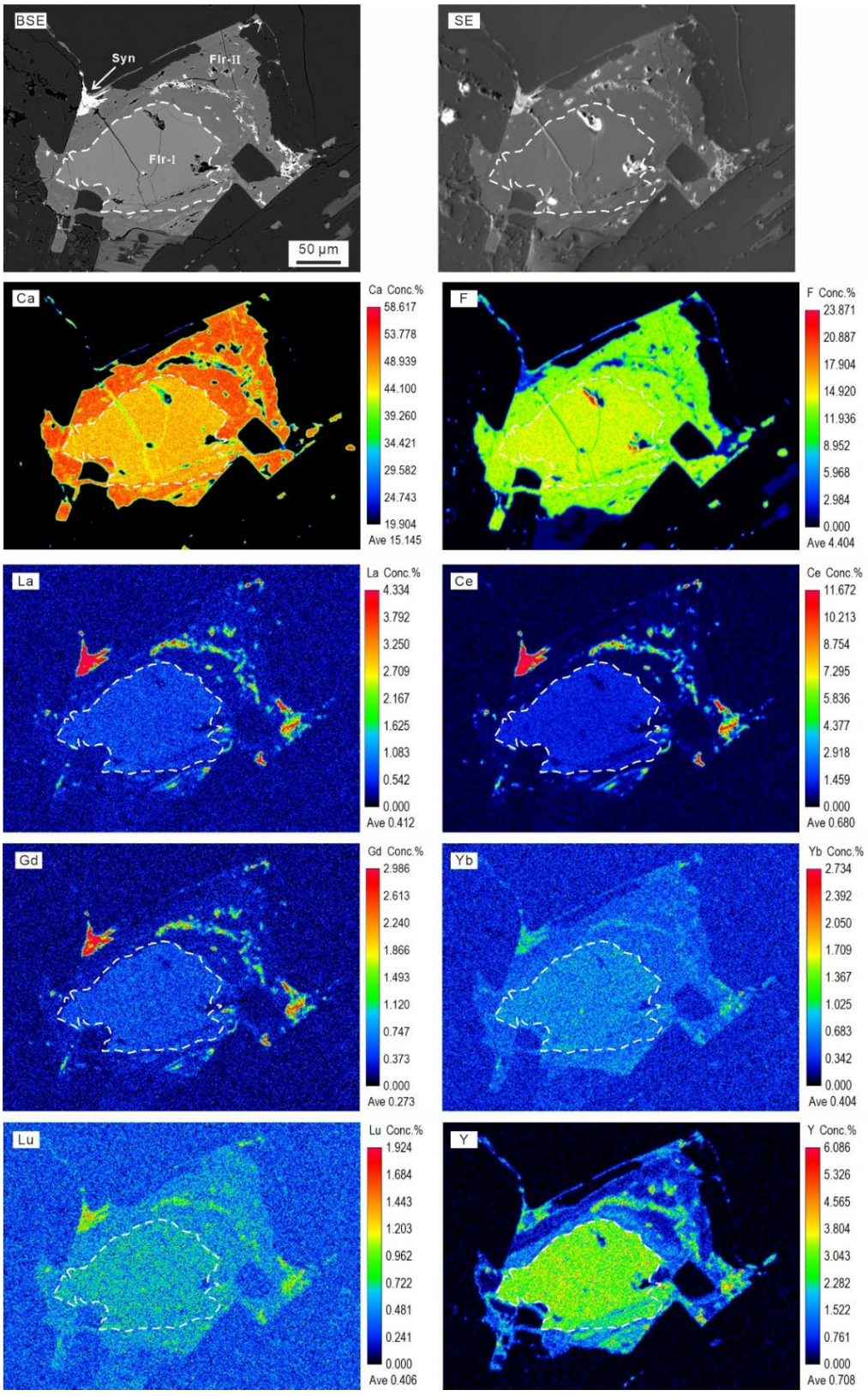
558

559 **Extended Data Fig. 4 | REE patterns of the Shitouping bedrock and regolith**

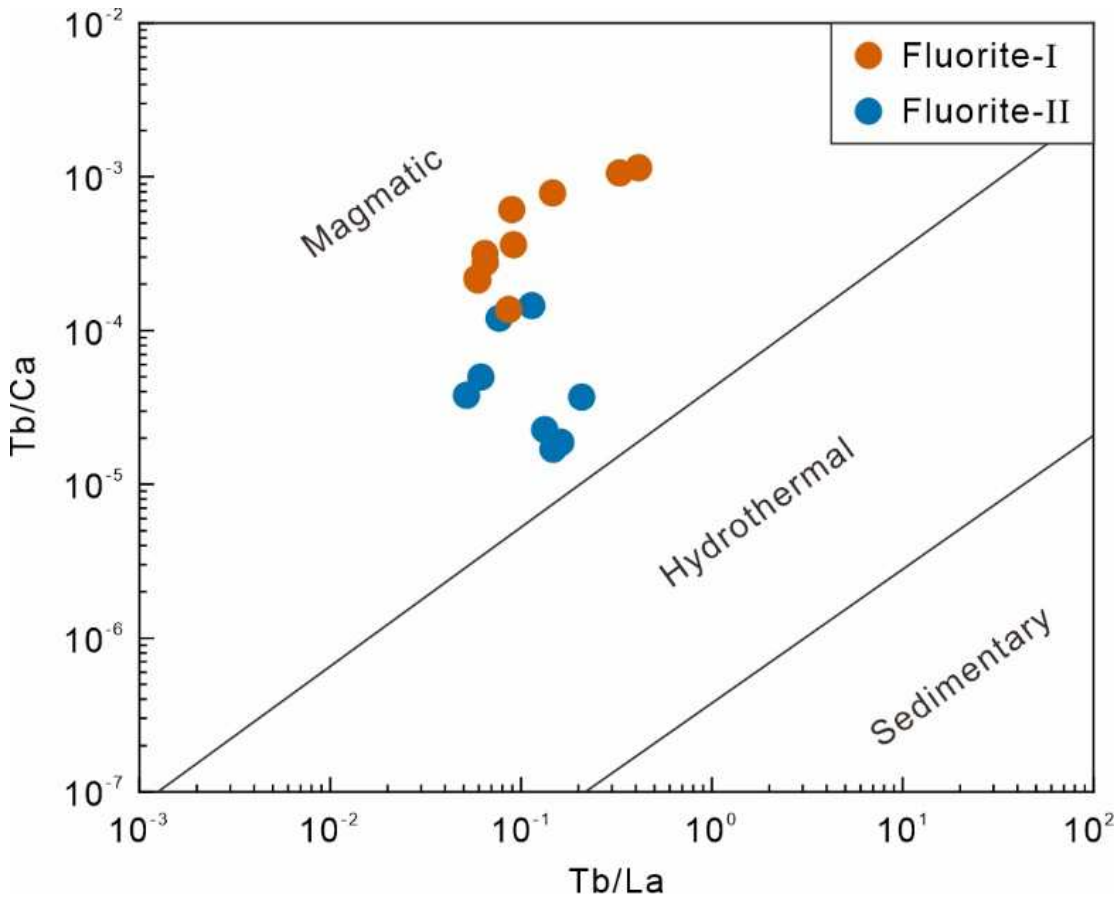
560 **samples.** Chondrite data after[55].



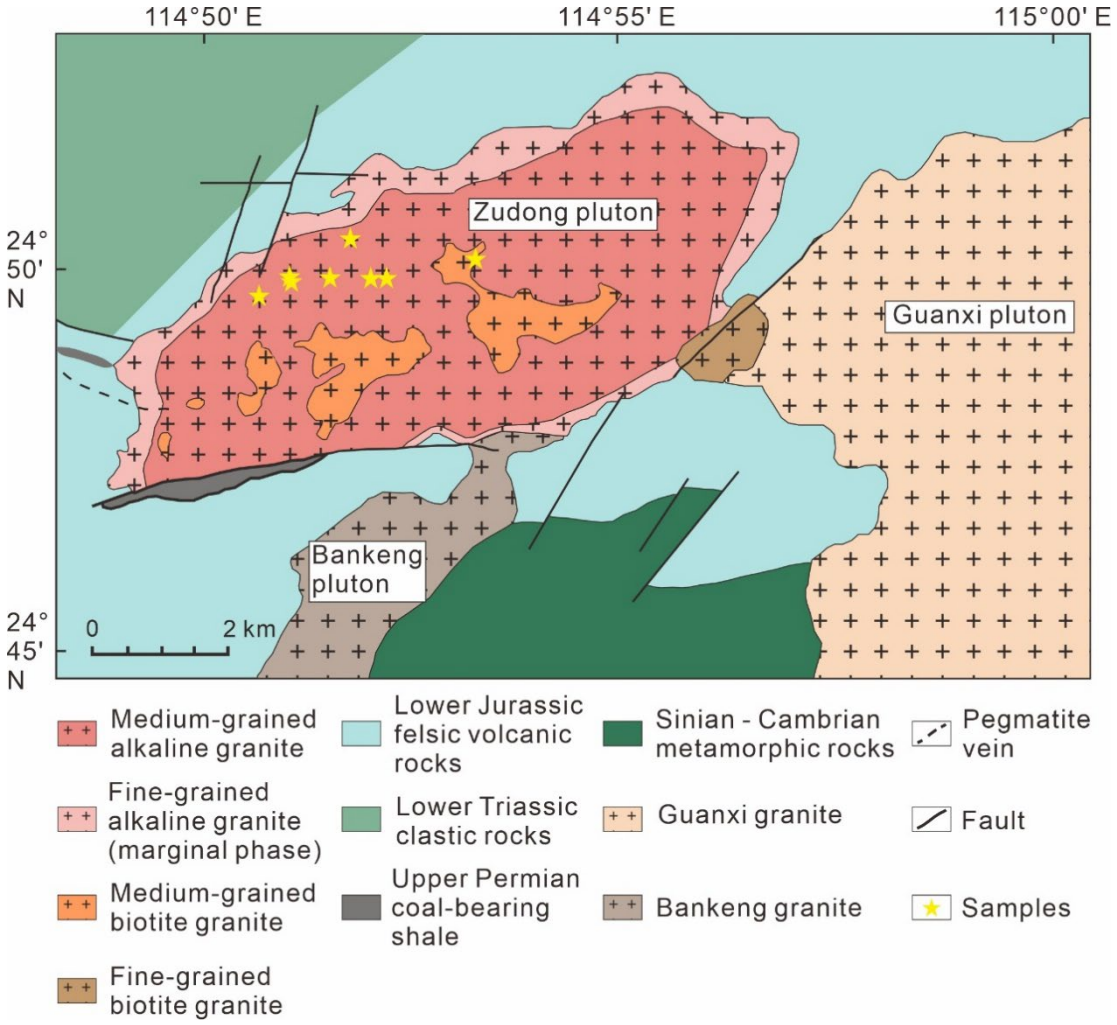
Extended Data Fig. 5 | Occurrence of fluorite in the bedrock. a–c, Optical photomicrographs: (**a**) and (**c**) in plane-polarized light, and (**b**) in cross-polarized light. **d**, Macrophotograph acquired using a digital camera. **e**,**f**, Backscattered electron images showing fluorite inclusions hosted in feldspar (**e**) and biotite (**f**), respectively. Abbreviations: Ab, albite; Bt, biotite; Flr, fluorite; Or, orthoclase; Qz, quartz; Syn, synchysite; Zrn, zircon.



Extended Data Fig. 6 | Electron probe microanalyzer (EPMA) wavelength dispersive spectroscopy (WDS) element maps of fluorite-synchysite aggregate. Elemental concentrations in the two fluorite varieties Flr-I and Flr-II differ markedly. Abbreviations: Flr, fluorite; Syn, synchysite.



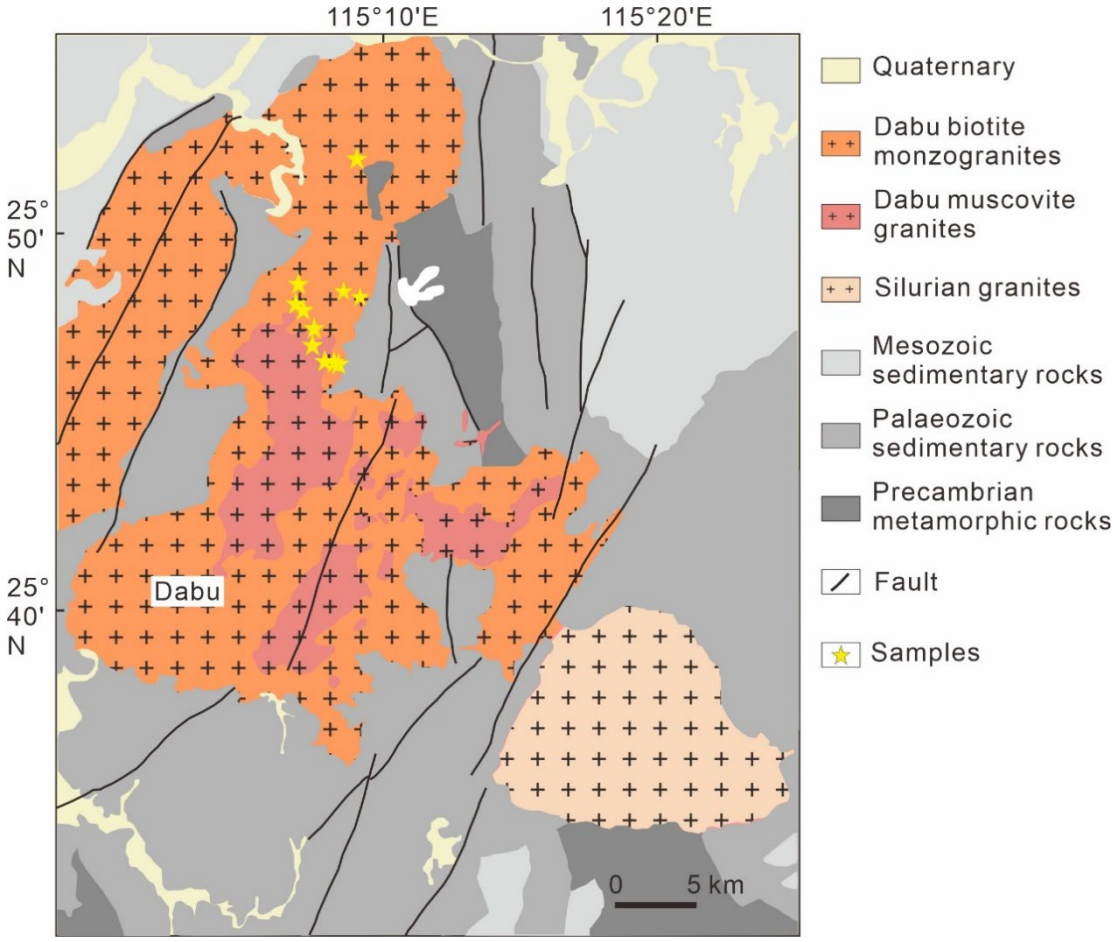
Extended Data Fig. 7 | Bivariate plot of fluorite Tb/Ca vs Tb/La. The fields for magmatic, hydrothermal, and sedimentary fluorite are from ref.[21,22], and the data are based on Supplementary Table 8.



577

578 **Extended Data Fig. 8 | Geological map of the Zuodong deposit (modified from**

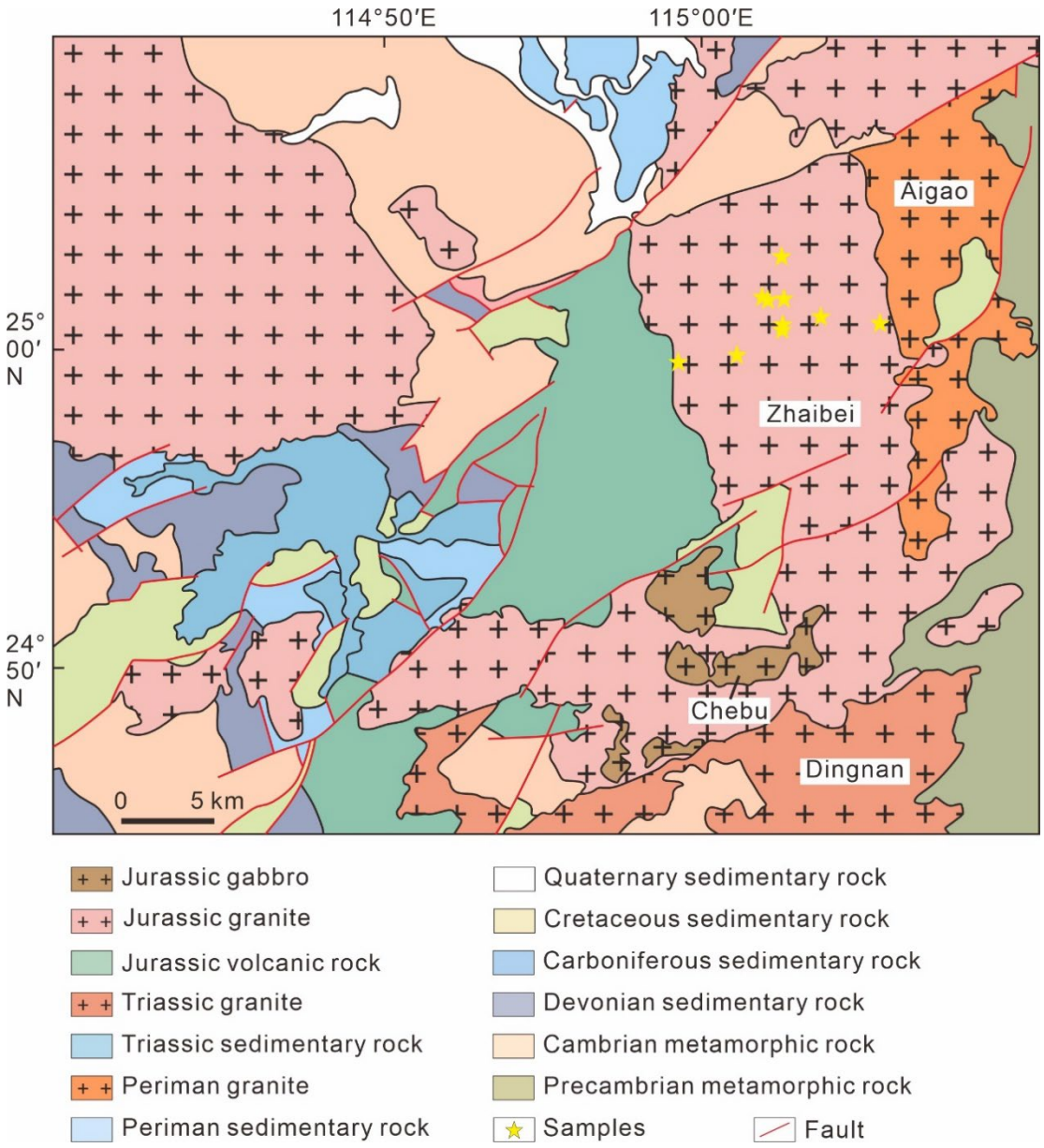
579 **ref.[15]) and sampling locations.**



580

581 **Extended Data Fig. 9 | Geological map of the Dabu deposit (modified from ref.[16])**

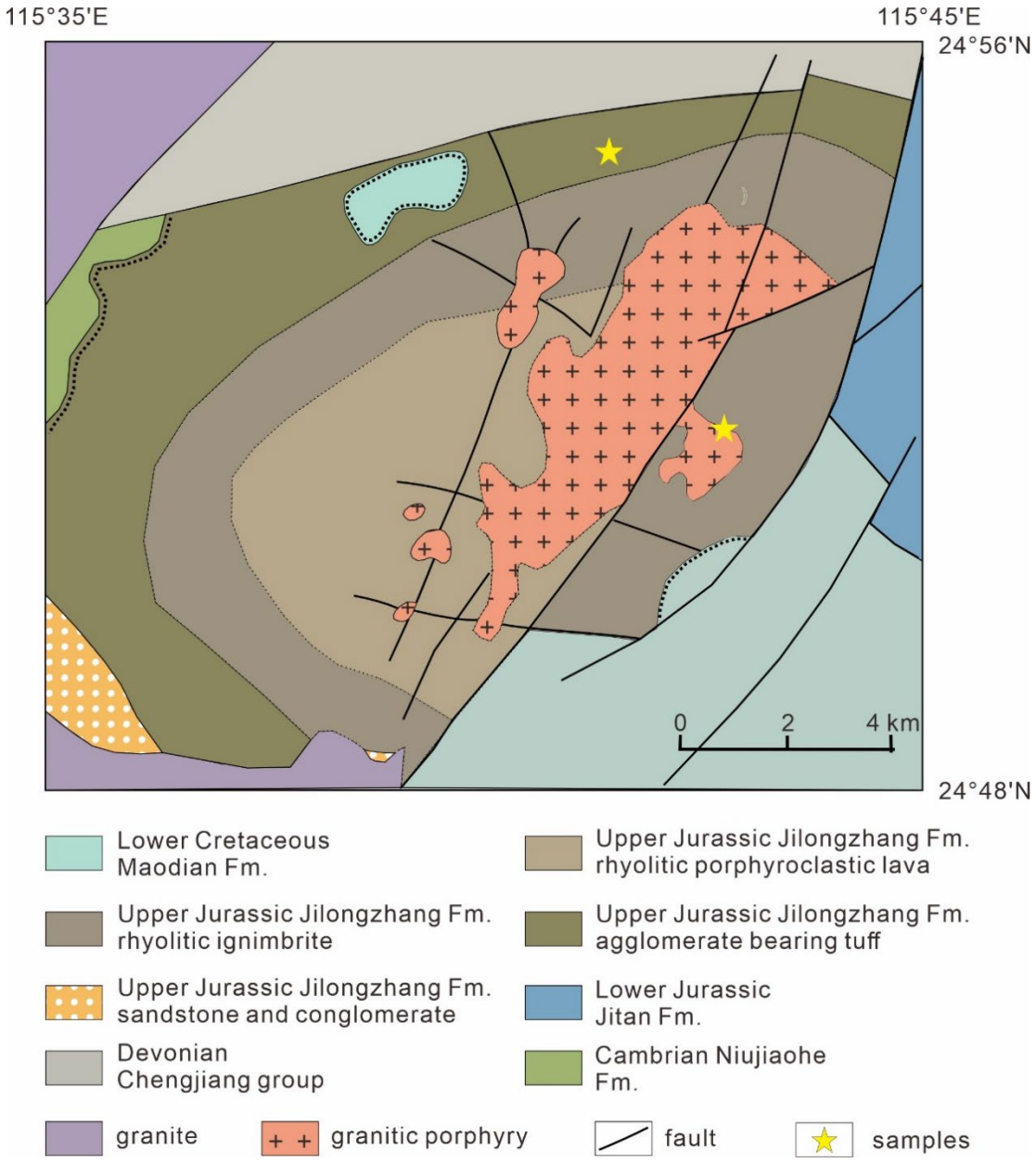
582 **and sampling locations.**



583

584 **Extended Data Fig. 10 | Geological map of the Zhaibei deposit modified from ref.[51])**

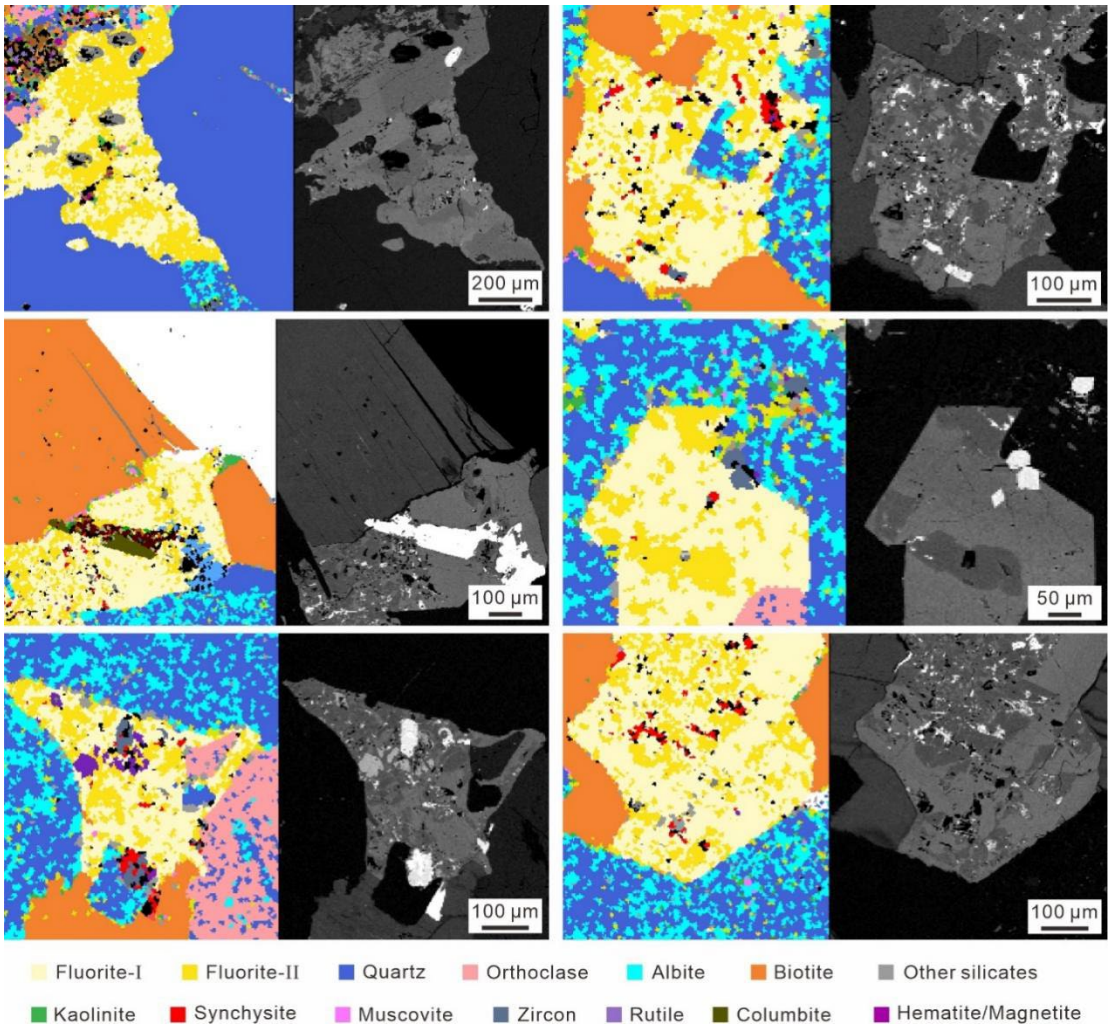
585 **and sampling locations.**



586

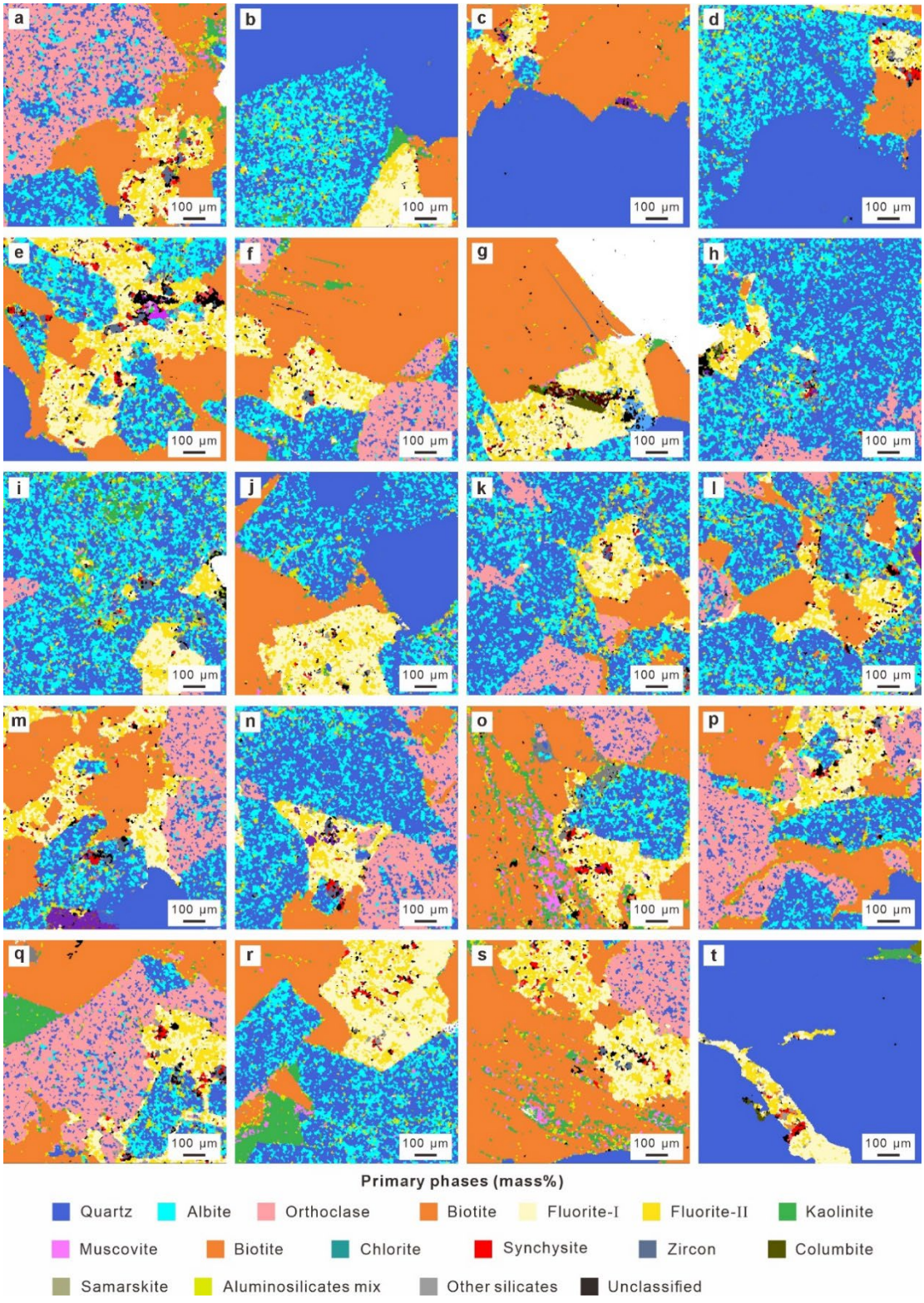
587 **Extended Data Fig. 11 | Geological map of the Heling deposit (modified from**

588 **ref.[17,56]) and sampling locations.**

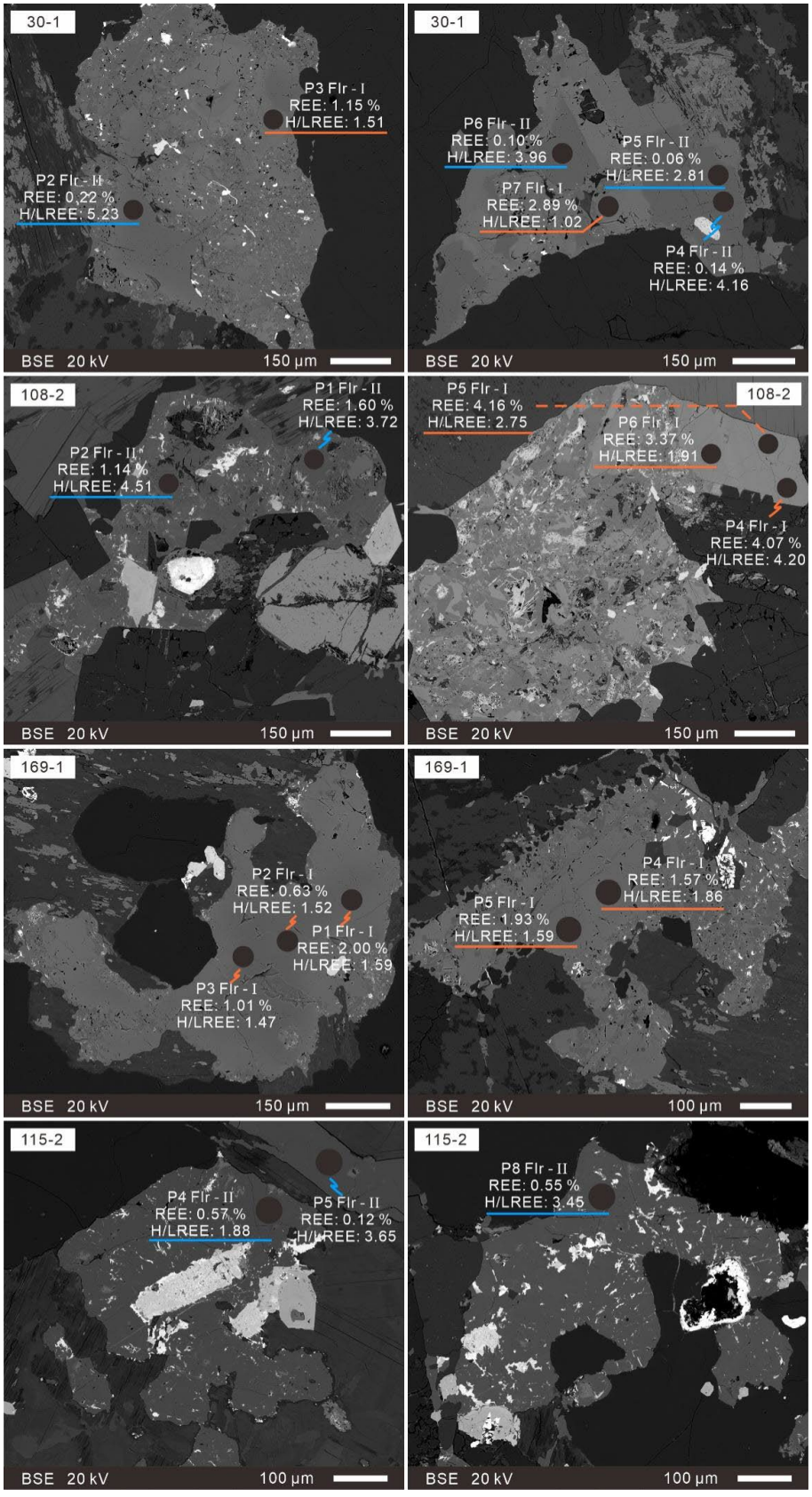


589

590 **Extended Data Fig. 12 | TESCAN TIMA results of fluorite and associated minerals**
591 **in comparison with backscatter electron images.** Colored images represent TIMA
592 results with mineral labels listed below; grey-scale images are backscatter electron
593 micrographs.



Extended Data Fig. 13 | Distribution of fluorite-I, fluorite-II, and synchysite. Mass balance calculations are listed in Supplementary Table 6.



Extended Data Fig. 14 | Fs-La analytical spots for two types of fluorite within the bedrock. Elemental concentrations in fluorite are provided in Supplementary Table 8.

Extended Data Table 1 | REE-bearing minerals in the bedrock of typical REE deposits

Area	REE-bearing minerals	Dominant	Ref.
Shitouping	fluorite, bastnäsite-(Ce) synchysite-(Y), xenotime, thorite	HREE	20
Zudong	fluorite, doverite, zircon, monazite, xenotime, niobite, pyrochlore, gadolinite	HREE	14
Dabu	fluorite, synchysite-(Y), garnet, zircon, fergusonite or pyrochlore-group, xenotime, thorite, monazite, gadolinite	HREE	16
HM granite	fluorite, synchysite-(Y), parisite-(Ce), apatite, zircon, xenotime-(Y), monazite-(Ce), Y-Ca silicate Y-Ti oxide	HREE	32
Zhaibei	fluorite, pyrochlore, garnet, zircon, thorite, xenotime, monazite, fergusonite, samarskite, gadolinite, aeschynite, euxenite Y-parisite	LREE	57
Heling	bastnäesite-(Ce), apatite, zircon, minor monazite, tourmaline, fergusonite, doverite, fluorite	LREE	17
Liberty Hill	titanite, apatite, monazite, zircon, allanite, bastnäsite	LREE	44
Serra Verde	REE-fluorocarbonates, fluorite, monazite-(Ce), xenotime-(Y), zircon, thorite,	LREE	45
Puxiong	bastnäsite-(Ce), parisite-(Ce), hiortdahlite, zircon, thorite, apatite, titanite, Nb-U-bearing minerals, cerite-(Ce), britholite-(Ce), tritomite-(Ce), monazite	LREE	52
Ambohimir-ahavavy	REE-fluorcarbonates, zirconosilicates, silicates and oxides with minor phosphates.	LREE	58

Supplementary Files

This is a list of supplementary files associated with this preprint. Click to download.

- SupplementaryTables.xlsx